Phagocytosis drives NAD^+ reduction-induced dendrite degeneration in *Drosophila*

Maria L. Sapar[1,2,3], Ankita Sarkar[1,3], Hui Ji[1,3], Bei Wang[1], and Chun Han[1*]

[1]Weill Institute for Cell and Molecular Biology and Department of Molecular Biology and Genetics, Cornell University, Ithaca, NY 14853, USA

[2]Current address: New York Stem Cell Foundation, New York, NY 10019, USA

[3]These authors contributed equally to this work

*Correspondence and Lead Contact: chun.han@cornell.edu

RUNNING TITLE

NAD^+ reduction in PS exposure-mediated dendrite degeneration

Keywords

phosphatidylserine, PS exposure, phagocytosis, phagocyte, Wallerian degeneration, dendrite degeneration, NAD^+, Nmnat, Sarm, calcium, *Drosophila*, da neuron,

ABSTRACT

During Wallerian degeneration, severed dendrites or axons expose the "eat-me" signal phosphatidylserine (PS) on their surface, thus initiating phagocytosis. Although neurite breakdown is believed to result from self-destruction, whether phagocytosis also contributes to Wallerian degeneration *in vivo* remain unknown. Here we show that in *Drosophila* sensory dendrites, phagocytosis is the main driver of dendrite degeneration induced by both genetic NAD^+ disruptions and injury. Specifically, NAD^+ reduction induced by Sarm activation in uninjured dendrites causes PS exposure and phagocytosis-dependent degeneration. In injured dendrites, PS-mediated phagocytosis is sufficient but not required for dendrite breakdown due to self-destruction triggered by catastrophic NAD^+ depletion. Surprisingly, axon-death factors Axed, Peb, and JNK signaling are not involved in neuronal PS exposure nor in dendrite self-destruction. Lastly, injured dendrites exhibit rhythmic calcium flashing, which is dependent on NAD^+ reduction. These results underscore the importance of phagocytosis in pathological neurite degeneration *in vivo*.

INTRODUCTION

Physical insults to the nervous system often disrupt neuronal connectivity and function by damaging dendritic or axonal processes of neurons. These injured neurites break down through a series of stereotypical events collectively called Wallerian degeneration (Waller, 1850; Coleman and Freeman, 2010). Before neurons can regenerate their processes and restore connections, the debris from damaged neurites has to be promptly cleared by phagocytes, which are cells that engulf dead cells or cell debris (Sapar and Han, 2019). Inefficient clearance can lead to neuroinflammation and further exacerbate the damage to the surrounding tissues (Davies et al., 2019; Galloway et al., 2019). Wallerian degeneration is mainly considered to be a neurite-intrinsic, self-destructive process (Gerdts et al., 2016) that *in vivo* is followed by phagocytic clearance. However, it remains unclear whether, under physiological conditions, phagocytosis actively contributes to neurite degeneration rather than simply passively removing neuronal debris.

Wallerian degeneration is governed by an evolutionarily conserved pathway, which is also called "axon-death" pathway because it was discovered in studies focused primarily on axon degeneration in *Drosophila* and rodents (Freeman et al., 2003; Gerdts et al., 2016; Sapar and Han, 2019). This pathway is centered on nicotinamide adenine dinucleotide (NAD^+), an essential cellular metabolite that is locally depleted after axons are injured. The signaling cascade starts with injury-induced activation of the E3

ubiquitin ligase Highwire/Phr1 in severed axons (Xiong et al., 2012; Babetto et al., 2013), which in turn causes degradation of nicotinamide mononucleotide adenyltransferase (Nmnat), an enzyme required for the synthesis of NAD^+ (Zhai et al., 2009). The resultant decrease of NAD^+ levels (Sasaki et al., 2016), likely together with accumulation of the NAD^+ precursor nicotinamide mononucleotide (NMN) (Di Stefano et al., 2015; Liu et al., 2018), activates Sarm/SARM1, a sterile alpha/Armadillo/Toll-Interleukin receptor homology domain protein (Osterloh et al., 2012). Sarm/SARM1 carries NADase activity; thus its activation causes catastrophic NAD^+ depletion, which drives axon breakdown through unclear mechanisms (Wang et al., 2005; Gerdts et al., 2015).

Besides this core Highwire/Phr1-Nmnat-NAD^+-Sarm/SARM1 pathway, several other factors have also been identified as acting in Wallerian degeneration. Downstream of *Sarm*, *axundead* (*axed*) is required for axon degeneration of olfactory receptor neurons (ORNs) and wing sensory neurons in *Drosophila* (Neukomm et al., 2017). The loss of *axed* blocks axon degeneration even when Sarm is dominantly activated, raising the possibility that Axed activation, rather than NAD^+ depletion, is the key switch of Wallerian degeneration (Neukomm et al., 2017). In addition, *pebbled* (*peb*) encodes a *Drosophila* transcription factor required for axon degeneration of glutamatergic but not cholinergic sensory neurons in the wing (Farley et al., 2018). Lastly, the dual leucine kinase (DLK)/c-Jun N-terminal kinase (JNK) stress pathway also contributes to, but is not required for, Wallerian degeneration in both *Drosophila* and mice (Miller et al., 2009; Yang et al., 2015). Although how these factors interact with the core components to promote axon degeneration is still mysterious, it is generally believed that catastrophic NAD^+ depletion caused by Sarm activity initiates a neurite-intrinsic self-destruction program that ultimately is responsible for Wallerian degeneration of axons (Babetto et al., 2013; Gerdts et al., 2015; Gerdts et al., 2016; Neukomm et al., 2017). While the Wallerian degeneration pathway is primarily characterized in axons, evidence suggests that NAD^+ reduction is also an essential step in injury-induced dendrite degeneration (Tao and Rolls, 2011; Sapar et al., 2018). However, which components of the Wallerian degeneration pathway are conserved in dendrites remains unknown.

Neuronal debris is recognized by resident phagocytes of the nervous system through specific "eat-me" signals exposed on the neuronal surface. A highly conserved eat-me signal is phosphatidylserine (PS), a negatively charged phospholipid normally found in the inner leaflet of the plasma membrane of healthy cells. During apoptosis, PS is externalized to the outer leaflet of the plasma membrane to mark the cell for engulfment (Leventis and Grinstein, 2010). Genetic evidence suggests that PS recognition is also important in neuronal clearance. In mice and zebrafish, certain PS-binding

bridging molecules and cell membrane receptors contribute to the phagocytosis of neurons (Nandrot et al., 2007; Mazaheri et al., 2014; Fourgeaud et al., 2016). Similarly, clearance of injured axons and dendrites in *Drosophila* requires Draper (Drpr), an engulfment receptor that binds to PS (Freeman et al., 2003; MacDonald et al., 2006; Tung et al., 2013; Han et al., 2014). Recently, PS exposure was directly observed on neurites undergoing Wallerian degeneration. Injured axons of mouse dorsal root ganglion (DRG) neurons show robust PS exposure in culture (Shacham-Silverberg et al., 2018). Interestingly, injured dendrites of *Drosophila* sensory neurons expose high levels of PS while they are degenerating and being engulfed (Sapar et al., 2018). A functional impact of neuronal PS exposure was demonstrated by ectopically induced PS exposure on otherwise healthy neurons, which resulted in engulfment-dependent neurite reduction in both the central nervous system (CNS) and the peripheral nervous system (PNS) (Sapar et al., 2018). These observations raise the question of whether PS-mediated phagocytosis contributes to Wallerian degeneration *in vivo*.

Recent studies suggest that neuronal PS exposure during Wallerian degeneration requires NAD^+ reduction. Overexpression of Wld^S, a fusion protein containing the full-length murine Nmnat1 (Mack et al., 2001), in *Drosophila* sensory neurons suppresses PS exposure of injured dendrites (Sapar et al., 2018). In addition, *Sarm1* ablation and NAD^+ supplementation in neuronal culture reduce PS exposure on injured axons (Shacham-Silverberg et al., 2018). The correlation of NAD^+ reduction with PS exposure suggests that phagocytosis may be more tightly associated with Wallerian degeneration than had been appreciated previously, a possibility that can be addressed by asking three important questions. First and foremost, does PS-mediated phagocytosis contribute to Wallerian degeneration *in vivo*? Second, how does NAD^+ reduction orchestrate both neuronal PS exposure and neurite self-destruction in time and space? Lastly, is PS exposure also regulated by other components of the Wallerian degeneration pathway, such as Axed, Peb, and JNK?

To address these questions, we utilized *Drosophila* class IV dendritic arborization (C4da) neurons on the larval body wall, an established *in vivo* model of injury-induced dendrite degeneration (Han et al., 2014). In this system, degenerating dendrites of C4da neurons are phagocytosed by epidermal cells through the engulfment receptor Drpr. By genetically manipulating NAD^+ levels and PS exposure in intact and injured dendrites, we show that, *in vivo*, phagocytosis is the main driving force of dendrite degeneration induced by NAD^+ reduction. Although NAD^+ reduction can cause both PS exposure and neurite self-destruction, a more severe NAD^+ reduction is required for activating self-destruction. Consequently, genetic ablation of *Nmnat* and injury result in dendrite degeneration through

different cellular mechanisms in membrane disruption, dendrite calcium dynamics, and phagocytosis dependence. Interestingly, injured dendrites exhibit unreported rhythmic calcium activities that may accelerate PS exposure or dendrite self-destruction. Lastly, neither *axed* nor *peb* nor the JNK pathway is involved in dendrite PS exposure or degeneration, suggesting that NAD^+ reduction is the only mechanism of Wallerian degeneration shared between dendrites and axons.

RESULTS

Nmnat knockout induces spontaneous dendrite degeneration due to Sarm-mediated NAD^+ reduction

NAD^+ reduction is required for PS exposure on injured dendrites (Sapar et al., 2018). To determine if NAD^+ loss is also sufficient to cause neuronal PS exposure, we decided to first investigate the impact of removing *Nmnat* from C4da neurons, as the loss of *Nmnat* is expected to cause cell-autonomous NAD^+ reduction. *Nmnat* LOF is known to induce degeneration of eye photoreceptors (Zhai et al., 2006) and wing sensory neurons (Neukomm et al., 2017). However, a previous study found that C4da neurons mutant for *Nmnat* did not show dendrite degeneration, despite displaying dendrite reduction and axon degeneration (Wen et al., 2011). To reexamine the LOF phenotype of *Nmnat*, we used CRISPR-TRiM, a tissue-specific mutagenesis method we previously developed (Poe et al., 2019), to knock out *Nmnat* in C4da neurons. In this method, *Nmnat* is knocked out by C4da-specific *ppk-Cas9* and two ubiquitously expressed guide-RNAs (gRNAs) targeting *Nmnat*. To distinguish dendrite reduction caused by degeneration from that caused by growth defects, we used CD4-tdTomato (CD4-tdTom) to label C4da dendrites. Because tdTom is stable in phagosomes, the presence of tdTom-labeled dendrite debris in epidermal cells is an indication of dendrite breakdown and subsequent engulfment (Han et al., 2014).

As expected, *Nmnat* knockout (KO) in C4da neurons (Figure 1B) caused strong dendritic reduction (Figure 1G) in wandering 3rd instar larvae as compared to the control (Figures 1A). In addition, dendrite debris was observed to spread in epidermal cells underneath and near the dendrites of *Nmnat* KO neurons (Figures 1B and 1H), suggesting that some dendrites had degenerated and were engulfed by epidermal cells. Unlike degenerating dendrites observed during developmental pruning or after injury (Han et al., 2011; Han et al., 2014), the remaining dendrites of *Nmnat* KO neurons did not show obvious blebbing or fragmentation, which may explain why dendrite degeneration was not detected previously in *Nmnat* mutant C4da neurons, considering that the membrane GFP marker used to

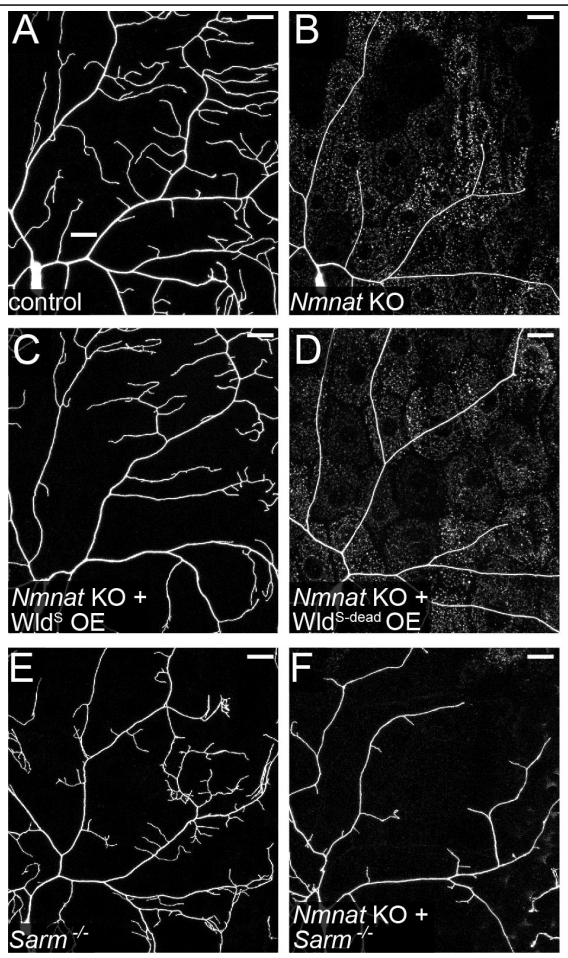

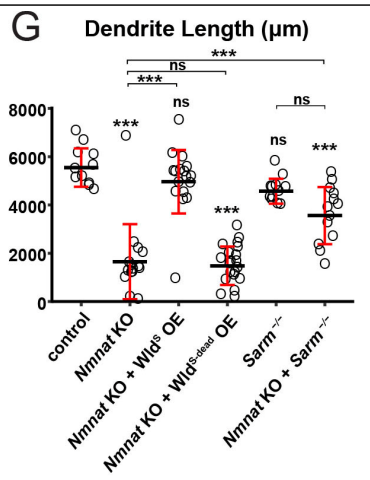

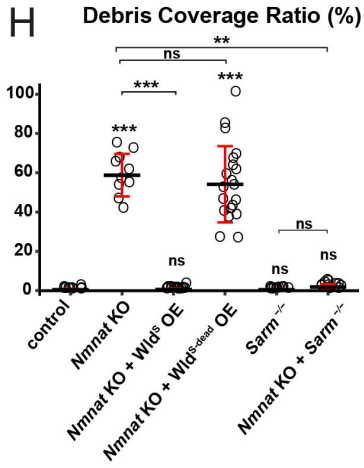

Figure 1: *Nmnat* knockout induces spontaneous dendrite degeneration due to Sarm-mediated NAD^+ reduction

(A-F) Partial dendritic fields of control (A), *Nmnat* KO (B), *Nmnat* KO + Wld^S OE (C), *Nmnat* KO + $Wld^{S\text{-dead}}$ OE (D), $Sarm^{4705/4621}$ (E), and *Nmnat* KO + $Sarm^{4705/4621}$ (F) ddaC C4da neurons. Neurons were labeled by *ppk>CD4-tdTom* (A-D) and *ppk-CD4-tdTom* (E and F). The C4da-specific KO was induced by *ppk-Cas9*. Scale bars, 25 μm.

(G) Quantification of dendrite length. n = number of neurons: control (n =11, 6 animals); *Nmnat* KO (n = 15, 9 animals); *Nmnat* KO + Wld^S OE (n = 17, 10 animals); *Nmnat* KO + $Wld^{S\text{-dead}}$ OE (n = 20, 11 animals); $Sarm^{4705/4621}$ (n = 12, 6 animals); *Nmnat* KO + $Sarm^{4705/4621}$ (n = 13, 9 animals). One-way ANOVA and Tukey's test.

(H) Quantification of debris coverage ratio, which is the percentage of debris area normalized by dendrite area ratio. n = number of neurons: control (n = 12, 6 animals); *Nmnat* KO (n = 10, 6 animals); *Nmnat* KO + Wld^S OE (n = 17, 10 animals); *Nmnat* KO + $Wld^{S\text{-dead}}$ OE (n = 20, 11 animals); $Sarm^{4705/4621}$ (n = 11, 6 animals); *Nmnat* KO + $Sarm^{4705/4621}$ (n = 13, 9 animals). Kruskal-Wallis (One-way ANOVA on ranks) and Dunn's test, p-values adjusted with the Benjamini-Hochberg method.

For all quantifications, **p≤0.01, ***p≤0.001; n.s., not significant. The significance level above each genotype is for comparison with the control. Black bar, mean; red bar, SD.

label dendrites in the previous study is rapidly degraded by epidermal cells once engulfed and thus cannot visualize phagosomes (Han et al., 2014).

Nmnat protects neurons by both synthesizing NAD^+ and functioning as a chaperon protein (Ali et al., 2013). To verify that the observed dendrite degeneration is due to the loss of Nmnat enzymatic activity, we tried to rescue *Nmnat* KO neurons by overexpressing Wld^S, which contains full NMNAT activity (Mack et al., 2001), and $Wld^{S\text{-dead}}$, a mutant version of Wld^S that cannot synthesize NAD^+ but maintains the chaperon function (Avery et al., 2009). Wld^S overexpression (OE) rescued the degeneration of *Nmnat* KO neurons and restored dendrite morphology to the wildtype level (Figures 1C, 1G, and 1H), while $Wld^{S\text{-dead}}$ OE did not change dendrite length or debris level of *Nmnat* KO neurons

(Figures 1D, 1G, and 1H). These results suggest that NAD^+ reduction is responsible for the dendrite degeneration of *Nmnat* KO neurons.

We next asked whether Sarm plays a role in *Nmnat* KO-induced dendrite degeneration. Indeed, *Sarm* LOF completely blocked dendrite degeneration of *Nmnat* KO neurons (Figures 1F, 1G, 1H), as evident in the absence of dendrite debris in epidermal cells. Some of these neurons showed reduced dendrites (Figures 1F and 1G) compared to *Sarm* LOF alone (Figures 1E, 1G, and 1H), likely due to the loss of Nmnat chaperon function (Wen et al., 2011). Importantly, these results demonstrate that *Sarm* is required for the dendrite degeneration of *Nmnat* KO neurons.

Lastly, we investigated a possible role for the JNK pathway in *Nmnat* KO-induced dendrite degeneration. Turning on the JNK pathway in C4da neurons by overexpressing the *Drosophila* dual leucine kinase Wallenda (Wnd) (Collins et al., 2006) caused a striking dendrite reduction without inducing degeneration (Figure 1 – figure supplement 1A, 1C, and 1D). Furthermore, knocking down *Drosophila JNK* in *Nmnat* KO neurons did not prevent dendrite degeneration (Figure 1 – figure supplement 1B, 1C, and 1D). Therefore, JNK signaling is detrimental to dendrite growth but does not contribute to *Nmnat* KO-induced dendrite degeneration.

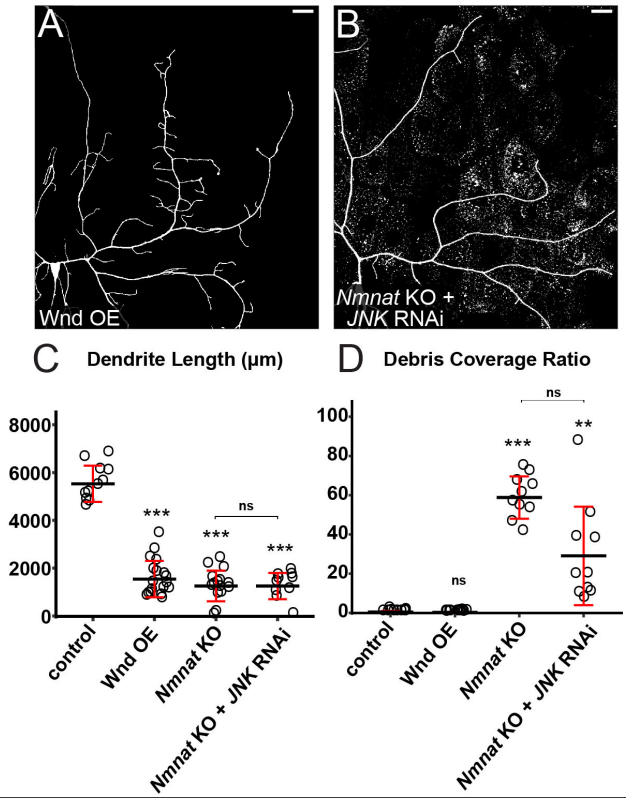

Figure 1 – figure supplement 1: The JNK pathway is not involved in spontaneous dendrite degeneration

(A-B) Partial dendritic fields of Wnd OE (A) and *Nmnat* KO + *JNK* RNAi (B) ddaC neurons. Neuronal labeling and CRISPR were done similarly to Figure 1. Neurons were labeled by *ppk>CD4-tdTom* and C4da-specific KO was induced by *ppk-Cas9*. Scale bars, 25 μm.

(C) Quantification of dendrite length. n = number of neurons: control (n = 11, 6 animals); Wnd OE (n =18, 10 animals); *Nmnat* KO (n = 15, 10 animals); *Nmnat* KO + *JNK* RNAi (n = 10, 6 animals). One-way ANOVA and Tukey's test.

(D) Quantification of debris coverage ratio. n = number of neurons: control (n = 12, 6 animals); Wnd OE (n = 18, 10 animals); *Nmnat* KO (n =10, 6 animals); *Nmnat* KO + *JNK* RNAi (n = 10, 6 animals). Kruskal-Wallis (One-way ANOVA on ranks) and Dunn's test, p-values adjusted with the Benjamini-Hochberg method.

For (C) and (D), the datasets for control and *Nmnat* KO are the same as in Figures 1G and 1H respectively. **p≤0.01, ***p≤0.001; n.s., not significant. The significance level above each genotype is for comparison with the control. Black bar, mean; red bar, SD.

All the results above together suggest that *Nnmat* LOF in neurons cause spontaneous dendrite degeneration through Sarm-mediated NAD^+ loss.

PS exposure-mediated phagocytosis causes dendrite degeneration of *Nmnat* KO neurons

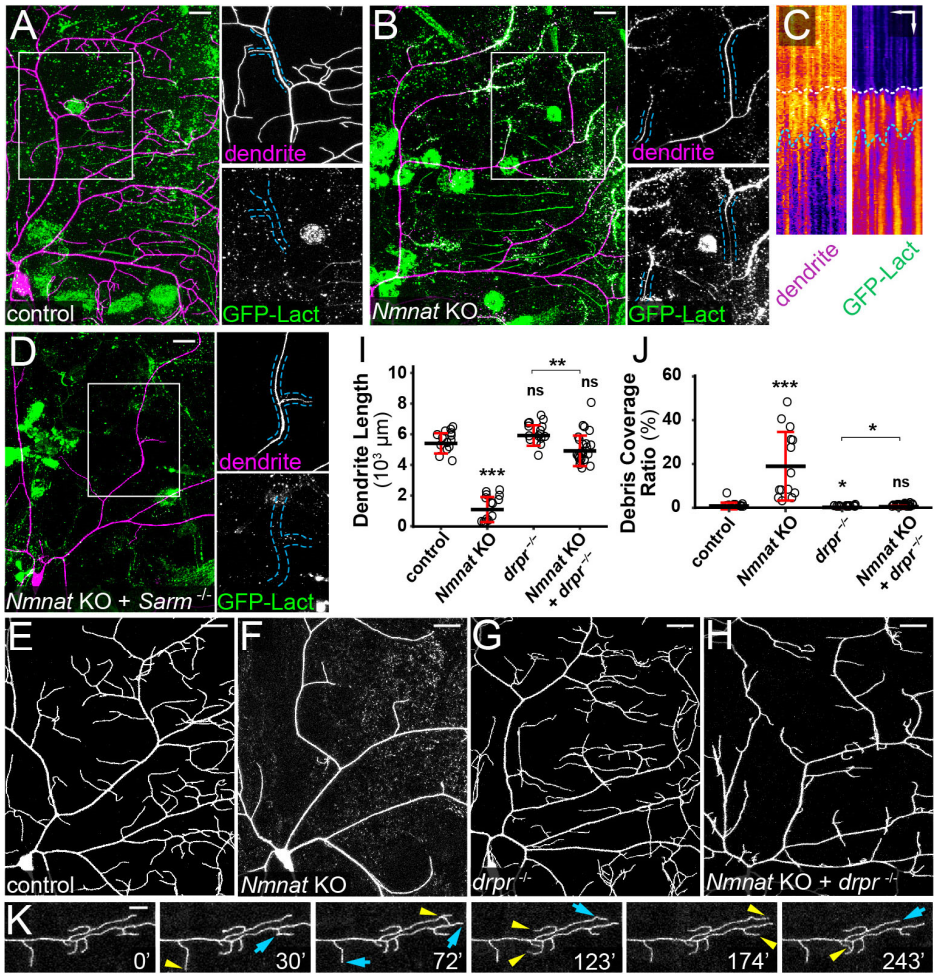

Figure 2: PS exposure-mediated phagocytosis causes dendrite degeneration of *Nmnat* KO neurons

(A) A control ddaC neuron showing the lack of GFP-Lact labeling. Insets show close-ups of an intact dendrite. Scale bar, 25 µm.

(B) A *Nmnat* KO ddaC neuron undergoing spontaneous degeneration and showing labeling by GFP-Lact. In the inset, the outlined dendrite segments do not show obvious blebbing or fragmentation but are weakly labeled by GFP-Lact. Scale bar, 25 µm.

(C) Kymographs of tdTom signal (dendrite) and GFP-Lact signal along a dendrite segment of a *Nmnat* KO ddaC neuron. White dotted lines indicate the timing of GFP-Lact initial binding to the dendrite; blue dotted lines indicate timing of the dendrite fragmentation based on the continuity of the dendrite signal. Scale bars, 10 µm horizontal, 60 min vertical. See also Video 1.

(D) Dendrites of a *Nmnat* KO + *Sarm*$^{4705/4621}$ ddaC neuron showing the lack of GFP-Lact labeling. Insets show close-ups of an intact dendrite. Scale bar, 25 µm.

(E-H) Partial dendritic fields of control (E), *Nmnat* KO (F), *drpr*$^{-/-}$ (G) and *Nmnat* KO + *drpr*$^{-/-}$ neurons. Scale bars, 25 µm.

(I) Quantification of dendrite length. n = number of neurons: control (n = 14, 7 animals); *Nmnat* KO (n = 14, 7 animals); *drpr*$^{-/-}$ (n = 16, 8 animals); *Nmnat* KO + *drpr*$^{-/-}$ (n = 24, 14 animals). One-way ANOVA and Tukey's test.

(J) Quantification of debris coverage ratio. n = number of neurons: control (n = 14, 7 animals); *Nmnat* KO (n =14, 7 animals); *drpr*$^{-/-}$ (n = 16, 8 animals); *Nmnat* KO + *drpr*$^{-/-}$ (n = 24, 14 animals). Kruskal-Wallis (One-way ANOVA on ranks) and Dunn's test, p-values adjusted with the Benjamini-Hochberg method.

(K) A time series of *Nmnat* KO + *drpr*$^{-/-}$ dendrites. Yellow arrowheads indicate growth of dendrites compared to the previous frame; blue arrows indicate retractions of dendrites compared to the previous frame. Scale bar, 10 µm. See also Video 2.

In all panels, neurons were labeled by *ppk-CD4-tdTom* and C4da-specific KO was induced by *ppk-Cas9*. For all quantifications, *p≤0.05, **p≤0.01, ***p≤0.001; n.s., not significant. The significance level above each genotype is for comparison with the control. Black bar, mean; red bar, SD.

To ask whether the NAD^+ loss induced by *Nmnat* KO also causes neuronal PS exposure, we used an established method to visualize PS exposure on C4da dendrites. In this method, the fluorescent PS sensor GFP-Lact is expressed by the larval fat body and secreted into the hemolymph (Sapar et al., 2018). As C4da dendrites are largely exposed to the hemolymph, GFP-Lact labeling allows visualization of dynamic PS exposure on dendrites in intact live animals (Sapar et al., 2018). We found that GFP-Lact strongly labeled *Nmnat* KO neurons at distal branches that underwent degeneration (Figure 2B), while wildtype C4da neurons showed no labeling (Figure 2A). Interestingly, we also observed weaker GFP-Lact labeling on dendrite segments that did not display obvious signs of degeneration (outlined in Figure 2B), suggesting that PS exposure may precede dendrite breakdown, instead of being merely a consequence of dendrite degeneration. This conclusion was further corroborated by time-lapse imaging of *Nmnat* KO neurons (Video 1) and kymograph analysis (Figure 2C): PS exposure (indicated by white dotted lines) occurred well ahead of dendrite fragmentation (indicated by blue dotted lines).

As *Sarm* is required for dendrite degeneration of *Nmnat* KO neurons, we asked if Sarm also regulates PS exposure in these neurons. *Nmnat* KO neurons showed no PS exposure in *Sarm* mutant background (Figure 2D), suggesting that Sarm-mediated NAD^+ reduction is also responsible for inducing the observed PS exposure.

The observation of PS exposure on *Nmnat* KO dendrites raises the question of whether PS exposure contributes to dendrite breakdown by inducing phagocytic attacks from epidermal cells. Because PS-mediated epidermal engulfment of dendrites requires Drpr (Sapar et al., 2018), we examined *Nmnat* KO dendrites in *drpr* mutant larvae. Strikingly, *drpr* LOF completely blocked dendrite degeneration of *Nmnat* KO neurons (Figure 2H as compared to Figures 2E-2G; Figures 2I and 2J). These dendrites exhibited dynamic extension and retraction behaviors (Figure 2K and Video 2), demonstrating that they were not fragmented dendrites that failed to be cleared.

Thus, our data demonstrate that phagocytic attack is responsible for dendrite degeneration of *Nmnat* KO neurons and NAD^+ reduction-induced PS exposure likely causes the phagocytic attack.

Wld^S OE and *Sarm* KO suppress PS exposure and fragmentation of injured dendrites

Wld^S protects injured neurites from degenerating by maintaining the NAD^+ level in the neurites. We previously found that overexpressing Wld^S in C4da neurons blocked fragmentation and PS exposure of ablated dendrites at 10 hrs after injury (AI) (Sapar et al., 2018). To further investigate the role of the Wallerian degeneration pathway in neuronal PS exposure, we examined the effects of overexpressing

192 Wld^S and knocking out *Sarm*, *axed*, or *peb* in C4da neurons at 24 hrs after laser-severing of dendrites.
193 Neuronal-specific KO was conducted using *SOP-Cas9*, which is active in precursor cells of da neurons,
194 to minimize potential gene perdurance (Poe et al., 2019). As expected, Wld^S OE blocked degeneration
195 and clearance of injured dendrites also at 24 hrs AI (Figure 3C, as compared to the control in Figure
196 3B), even though the injured arbors were greatly simplified as compared to uninjured dendrites (Figures
197 3A and 3E). Neuronal-specific *Sarm* KO showed similar effects in injured dendrites (Figures 3D and

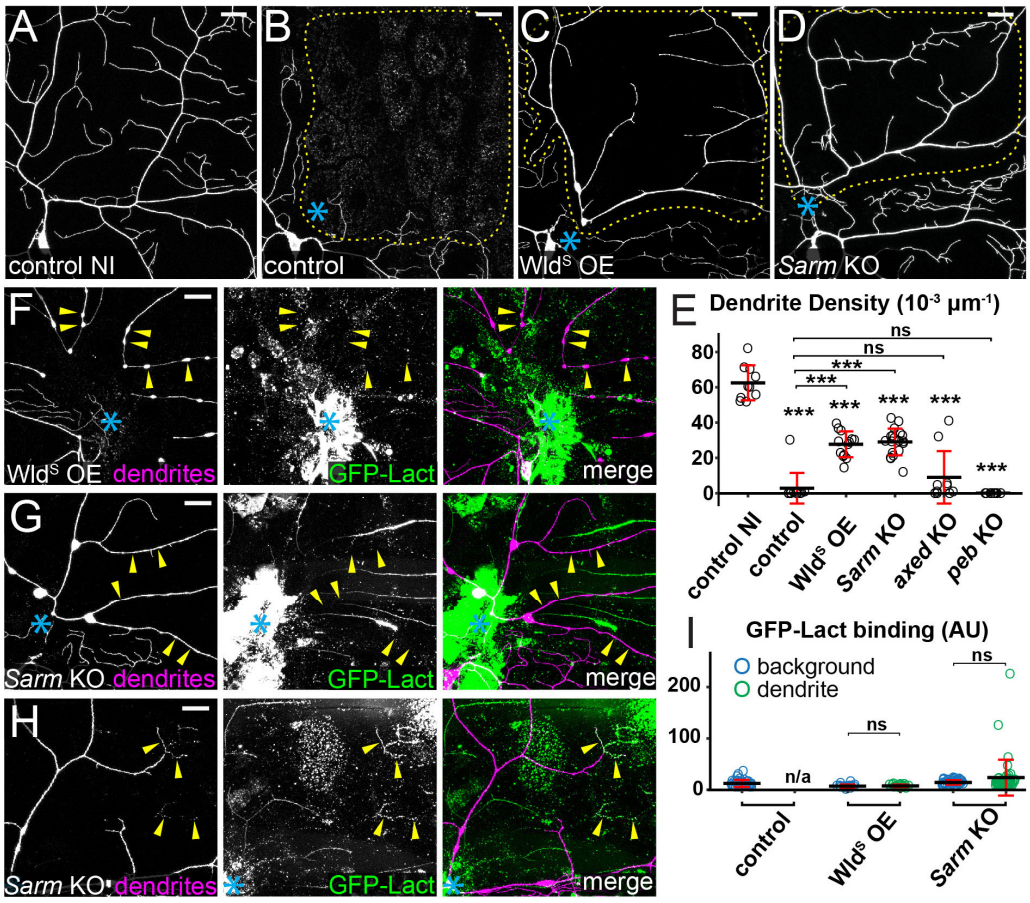

Figure 3: Wld^S OE and *Sarm* KO suppress PS exposure and fragmentation of injured dendrites

(A) Partial dendritic field of an uninjured ddaC control neuron.

(B-D) Partial dendritic fields of control (B), Wld^S OE (C) and *Sarm* KO (D) ddaC neurons 24 hrs after injury (AI). Blue asterisk, injury site. Yellow dots outline regions covered by injured dendrites.

(E) Quantification of dendrite density (1000 x dendritic length/area) in regions covered by injured dendrites. n = number of neurons: control no injury (NI) (n = 10, 10 animals); control (n = 12, 6 animals); Wld^S OE (n = 13, 6 animals); *Sarm* KO (n = 19, 6 animals); *axed* KO (n = 10, 5 animals); *peb* KO (n = 12, 7 animals).

(F and G) Wld^S OE (E) and *Sarm* KO (F) ddaC neurons 24 hrs AI, showing unfragmented dendrites and lack of GFP-Lact binding to severed dendrites (yellow arrowheads).

(H) Dendrites of a *Sarm* KO ddaC neuron 24 hrs AI, showing infrequent GFP-Lact binding at fragmented terminal branches (yellow arrowheads).

(I) Quantification of GFP-Lact binding on injured dendrites. The GFP-Lact intensity is shown for both background epidermal regions and injured dendrites. The outliers in *Sarm* KO dendrite dataset correspond to infrequent degenerating terminal branches. Background: epidermal regions without dendrites. n = number of measurements: control background (n = 39) and control dendrite (n/a, no remaining dendrites), 7 animals; Wld^S OE background (n = 18) and Wld^S OE dendrite (n = 18), 4 animals; *Sarm* KO background (n = 48) and *Sarm* KO dendrite (n = 48), 9 animals.

In all panels, neurons were labeled by *ppk>CD4-tdTom* (D), *ppk-CD4-tdTom* (E-G), and *ppk-MApHS* (A, B, C; only tdTom channel is shown). Neuronal-specific KO was induced by *SOP-Cas9*. For all quantifications, One-way ANOVA and Tukey test; ***p≤0.001; n.s., not significant; n/a., not applicable. The significance level above each genotype in (E) is for comparison with the control. Black bar, mean; red bar, SD. Scale bars, 25 µm.

198 3E) to those of Wld^S OE. Interestingly, neuronal KO of *axed* did not prevent degeneration of injured
199 dendrites (Figures 3E and Figure 3 – figure supplement 1H). This lack of defects is unlikely due to
200 inefficient CRISR-TRiM, as knocking out *axed* using the same gRNAs in Or22a olfactory neurons, an
201 established axon-injury model (MacDonald et al., 2006), effectively blocked degeneration of severed
202 axons 7 days after antenna ablation (Figure 3 – figure supplement 1A-1D, and 1G). Similarly, we did not
203 observe degeneration defects in *peb* KO neurons (Figures 3E, and Figure 3 – figure supplement 1J),
204 even though *peb* KO appeared to cause dendrite reduction in C4da neurons (Figure 3 – figure
205 supplement 1I). Unexpectedly, knocking out *peb* from precursors of Or22a neurons caused loss of some
206 or all of Or22a axons in uninjured adult brains (Figure 3 – figure supplement 1E and 1G), suggesting
207 that *peb* plays a role in Or22a development or axon patterning. The remaining axons of *peb* KO neurons
208 did not show defects in axon degeneration after injury (Figure 3 – figure supplement 1F and 1G). These
209 results suggest that unlike Sarm, Axed and Peb may be neuronal type-specific modulators of the
210 Wallerian degeneration pathway and are not required for dendrite degeneration of da neurons.

211 We next examined the effects of Wld^S OE and *Sarm* KO on dendritic PS exposure 24 hrs AI, as
212 they were the only manipulations that blocked degeneration of injured dendrites. Wld^S OE prevented PS
213 exposure on severed dendrites, even on branches that showed blebbing and breakage (Figures 3F and
214 3I). *Sarm* KO also effectively blocked PS exposure on injured dendrites (Figures 3G and 3I), with

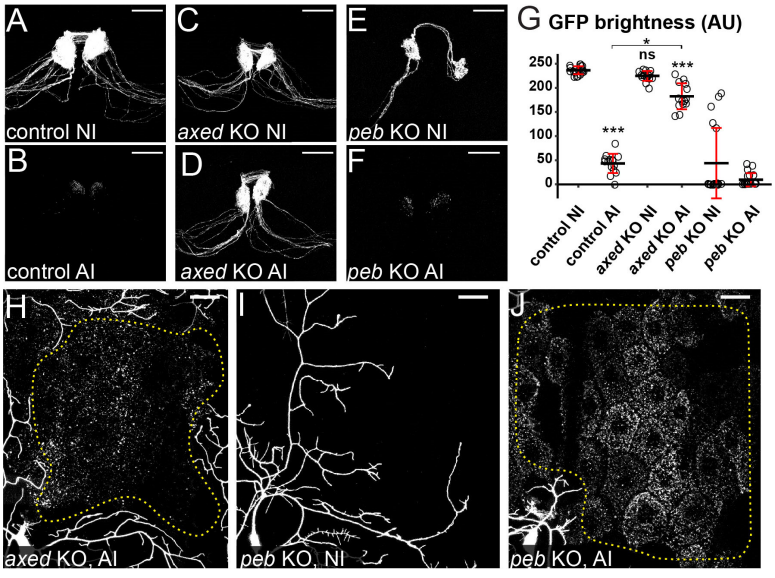

Figure 3 – figure supplement 1: *axed* KO and *peb* KO do not block degeneration and clearance of injured dendrites

(A-F) Axons of control NI (A), control 7 days AI (B), *axed* KO NI (C), *axed* KO 7 days AI (D), *peb* KO NI (E), *peb* KO 7 days AI (F) Or22a neurons in 14-day-old adult brains. Or22a neurons were labeled by *Or22a>CD8-GFP* and KO was induced by *ey-Cas9*. Scale bars, 25 μm.

(G) Quantification of GFP brightness of Or22a glomeruli. n = number of brains: control NI 14 days (n = 19); control 7days AI 14 days (n = 15); *axed* KO NI 14 days (n = 16); *axed* KO 7 days AI 14 days (n = 14); *peb* KO NI 14 days (n = 18); *peb* KO 7 days AI 14 days (n = 20). Kruskal-Wallis (One-way ANOVA on ranks) and Dunn's test, p-values adjusted with the Benjamini-Hochberg method. *p≤0.05, ***p<0.001, n.s., not significant. The significance level above each genotype is for comparison with the control. Statistical comparisons for *peb* KO glomeruli are not shown due to the variation within the group of *peb* KO NI 14 days. Black bar, mean; red bar, SD.

(H-J) Partial dendritic fields of *axed* KO 24 hrs AI (H), *peb* KO NI (I), *peb* KO 24 hrs AI (J) and control 24 hrs AI (K) ddaC neurons. Yellow dots outline regions covered by injured dendrites in (H) and (J). Neurons were labeled by *ppk>CD4-tdTom* and neuronal-specific KO was induced by *SOP-Cas9*. Scale bars, 25 μm.

occasionally strong PS labeling on fragmentated distal terminal branches (Figures 3H and 3I). The above data in dendrite injury together suggest that Sarm-mediated NAD^+ reduction causes both PS exposure and degeneration of injured dendrites. The PS exposure on fragmented terminal dendrites of *Sarm* KO neurons could be due to relatively faster NAD^+ turnover in those local branches even in the absence of Sarm.

Ectopic PS exposure causes injured dendrites of Wld^S OE and *Sarm* KO neurons to degenerate

The absence of PS exposure on injured dendrites of Wld^S OE and *Sarm* KO neurons raises the question of whether the degeneration defects of these neurons are due to the lack of PS-mediated epidermal attack on dendrites. To test this hypothesis, we ectopically induced neuronal PS exposure by knocking out *CDC50*, which encodes a chaperone necessary for the function of *Drosophila* flippases (Tanaka et al., 2011), and by overexpressing TMEM16F, a mammalian PS scramblase (Segawa et al., 2011). These manipulations in C4da neurons cause mild but appreciable phagocytosis-dependent dendrite loss (Sapar et al., 2018). *CDC50* KO or TMEM16F OE alone in Wld^S OE neurons caused partial or complete degeneration of injured dendrites and the accompanying epidermal engulfment (Figures 4A, 4B, and 4E). A much stronger effect was observed when *CDC50* KO and TMEM16F OE were combined in Wld^S OE neurons: Degeneration and clearance of injured dendrites were restored to the wildtype level

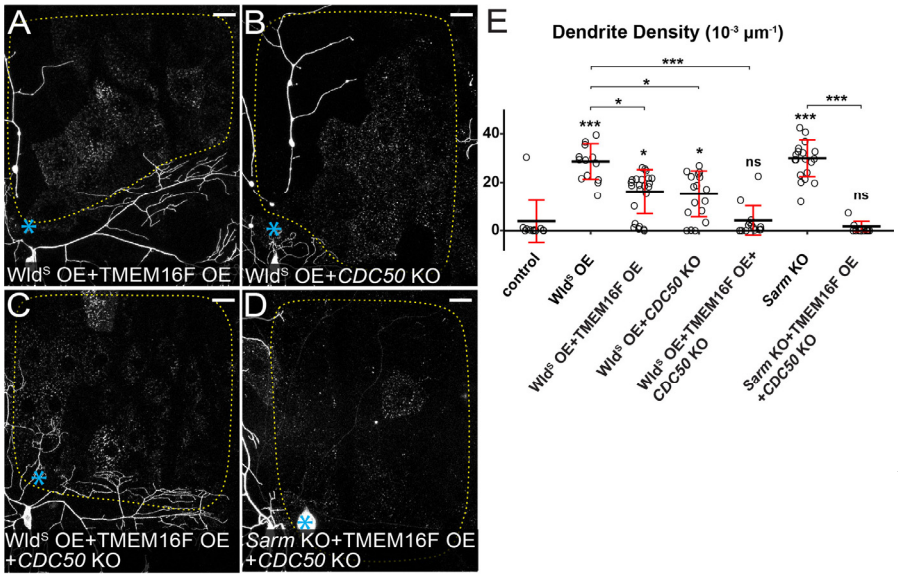

Figure 4: Ectopic PS exposure causes injured dendrites of Wld^S OE and *Sarm* KO neurons to degenerate.

(A-D) Partial dendritic fields of Wld^S OE + TMEM16F OE (A), Wld^S OE + *CDC50* KO (B), Wld^S OE + TMEM16F OE + *CDC50* KO (C) and *Sarm* KO + TMEM16F OE + *CDC50* KO (D) ddaC neurons 24 hrs AI. Blue asterisk, injury site. Yellow dots outline regions covered by injured dendrites. Neurons were labeled by *ppk-MApHS* (A, B, and C) and *ppk-CD4-tdTom* (D). Neuronal-specific KO was induced by *ppk-Cas9* (B and C) and *SOP-Cas9* (D). Scale bars, 25 µm.

(E) Quantification of dendrite density. n = number of neurons: control (n = 12, 6 animals); Wld^S OE (n = 13, 6 animals); Wld^S OE + TMEM16F OE (n = 23, 8 animals); Wld^S OE + *CDC50* KO (n = 17, 8 animals); Wld^S OE + TMEM16F OE + *CDC50* KO (n = 16, 8 animals); *Sarm* KO (n = 19, 6 animals); *Sarm* KO + TMEM16F OE + *CDC50* KO (n = 13, 7 animals). Kruskal-Wallis (One-way ANOVA on ranks) and Dunn's test, p-values adjusted with the Benjamini-Hochberg method. The dataset for Wld^S OE and *Sarm* KO is the same as in Figure 3E.

For all quantifications, *p≤0.05, ***p≤0.001; n.s., not significant. The significance level above each genotype is for comparison with the control. Black bar, mean; red bar, SD.

(Figures 4C and 4E). Similarly, *CDC50* KO and TMEM16F OE caused injured dendrites of *Sarm* KO neurons to completely degenerate (Figures 4D and 4E). Because injury induces a more rapid and stronger PS exposure on dendrites than *CDC50* KO or TMEM16F OE (Sapar et al., 2018), our data strongly suggest that injury-induced PS exposure is a major driver of dendrite breakdown by activating phagocytic attack by epidermal cells.

Injury and NAD^+ depletion cause phagocytosis-independent dendrite self-destruction

Although PS-mediated phagocytosis is sufficient to break down injured dendrites, blocking phagocytosis with *drpr* LOF failed to prevent the fragmentation of injured dendrites 20 hrs AI, even though the dendrite debris was left unengulfed (Figures 5A-5C). This suggests that factors other than PS exposure can cause phagocytosis-independent dendrite fragmentation after injury. To understand why *drpr* LOF efficiently blocked dendrite degeneration of *Nmnat* KO neurons but failed to prevent breakdown of injured dendrites, we examined potential contributions of JNK signaling, as JNK signaling is turned on in injured neurites (Yang et al., 2015) but not in *Nmnat* KO neurons (Figure 1 – figure supplement 1). However, overexpressing Wnd in *Nmnat* KO neurons did not lead to dendrite degeneration in *drpr* mutant, even though it caused strong dendrite reduction (Figure 5 – figure supplement 1A-1C). Conversely, expressing a dominant negative JNK in neurons did not prevent fragmentation of injured

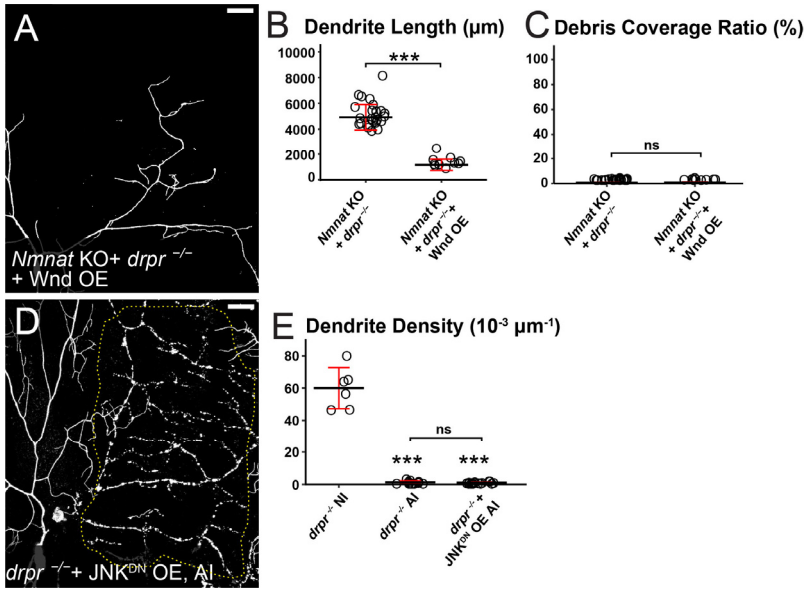

Figure 5 – figure supplement 1: The JNK stress pathway is not involved in dendrite self-destruction

(A) Partial dendritic field of a *Nmnat* KO + $drpr^{-/-}$ + Wnd OE ddaC neuron.

(B) Quantification of dendrite length. n = number of neurons: *Nmnat* KO + $drpr^{-/-}$ (n = 24, 13 animals); *Nmnat* KO + $drpr^{-/-}$ + Wnd OE (n = 10, 8 animals).

(C) Quantification of debris coverage ratio. n = number of neurons: *Nmnat* KO + $drpr^{-/-}$ (n = 24, 13 animals); *Nmnat* KO + $drpr^{-/-}$ + Wnd OE (n = 10, 8 animals).

(D) Partial dendritic field of a $drpr^{-/-}$ + JNK^{DN} OE ddaC neuron 24 hrs AI.

(E) Quantification of dendrite density. n = number of neurons: $drpr^{-/-}$ NI (n = 6, 5 animals); $drpr^{-/-}$ AI (n = 13, 5 animals); $drpr^{-/-}$ + JNK^{DN} OE AI (n = 16, 9 animals). Neurons were labeled by *ppk>CD4-tdTom* (A) and *ppk-CD4-tdTom* (D), C4da-specific KO was induced by *ppk>Cas9*, JNK^{DN} OE was driven by $Gal4^{21-7}$ (D). For all quantifications, ***p≤0.001; n.s., not significant; Welch's t-test (B and C) and Kruskal-Wallis (One-way ANOVA on ranks) and Dunn's test, p-values adjusted with the Benjamini-Hochberg method (E). The significance level above each genotype in (E) is for comparison with the control. Black bar, mean; red bar, SD. Scale bars, 25 μm.

dendrites in *drpr* mutant (Figure 5 – figure supplement 1D and 1E). These results argue that JNK signaling is not the cause of phagocytosis-independent dendrite fragmentation after injury.

A neurite self-destruction program triggered by NAD^+ depletion has been thought to be responsible for Wallerian degeneration (Gerdts et al., 2015). To test the possibility that a further NAD^+ reduction beyond the level that triggers PS exposure caused phagocytosis-independent dendrite self-destruction, we tested the effect of overexpressing a gain-of-function Sarm ($Sarm^{GOF}$) in C4da neurons, because $Sarm^{GOF}$ potently depletes NAD^+ and causes dominant neurodegeneration (Neukomm et al., 2017). Indeed, $Sarm^{GOF}$ OE caused complete dendrite degeneration in most neurons as early as 24 hrs after egg laying (AEL) (Figures 5D and 5J), while *Nmnat* KO did not cause dendrite degeneration until 88-91 hrs AEL. Supporting the role of engulfment in NAD^+ reduction-induced dendrite degeneration, *drpr* LOF strongly suppressed dendrite degeneration of $Sarm^{GOF}$ OE neurons at both 24 hrs AEL and 48

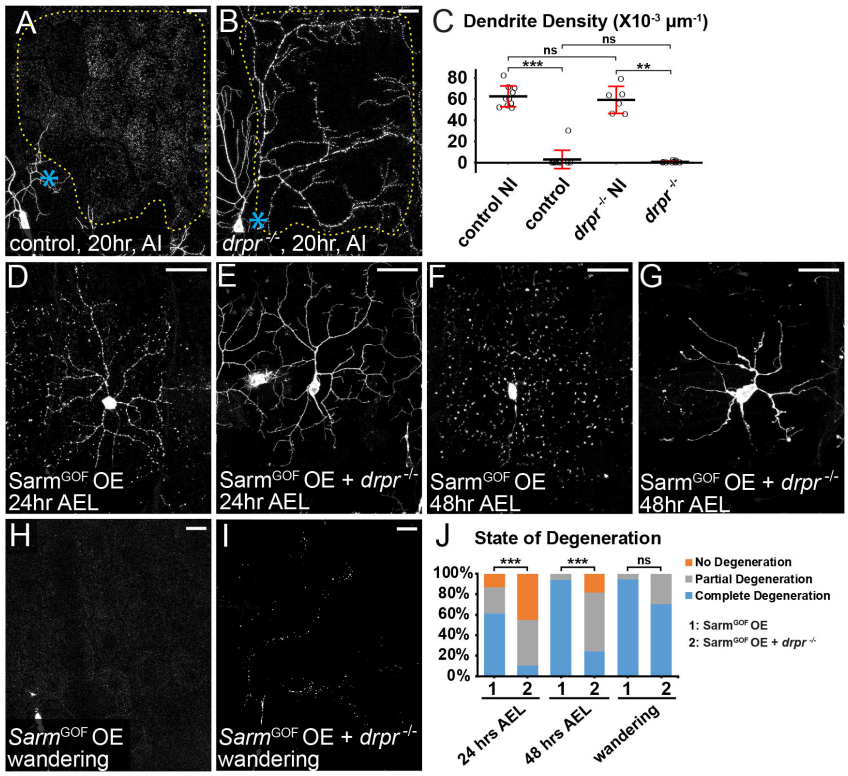

Figure 5: Injury and NAD^+ depletion cause phagocytosis-independent dendrite self-destruction

(A-B) Partial dendritic fields of ddaC neurons in control (A) and *drpr*$^{-/-}$ (B) animals 20 hrs AI. The dendrite debris lining up in the original dendritic pattern in (B) indicates dendrite fragmentation and the lack of epidermal engulfment. Blue asterisk, injury site. Yellow dots outline regions covered by injured dendrites.

(C) Quantification of dendrite density. n = number of neurons: control no-injury (NI) (n = 10, 10 animals); control AI (n = 12, 6 animals); *drpr*$^{-/-}$ NI (n = 6, 5 animals); *drpr*$^{-/-}$ AI (n = 13, 5 animals). Kruskal-Wallis (One-way ANOVA on ranks) and Dunn's test, p-values adjusted with the Benjamini-Hochberg method.

(D-G) ddaC neurons in *Sarm*^{GOF} OE 24 hrs after egg laying (AEL) (D), *Sarm*^{GOF} OE + *drpr*$^{-/-}$ 24 hrs AEL (E), *Sarm*^{GOF} OE 48 hrs AEL (F) and *Sarm*^{GOF} OE + *drpr*$^{-/-}$ 48 hrs AEL (G).

(H-I) Partial dendritic fields of *Sarm*^{GOF} OE (H) and *Sarm*^{GOF} OE + *drpr*$^{-/-}$ (I) ddaC neurons at the wandering stage.

(J) Quantification of dendrite degeneration showing percentages of neurons undergoing partial degeneration, complete degeneration and no degeneration. n = number of neurons: *Sarm*^{GOF} OE 24 hrs AEL (n = 31, 7 animals); *Sarm*^{GOF} OE + *drpr*$^{-/-}$ 24 hrs AEL (n = 49, 17 animals); *Sarm*^{GOF} OE 48 hrs AEL (n = 17, 7 animals); *Sarm*^{GOF} OE + *drpr*$^{-/-}$ 48 hrs AEL (n = 33, 11 animals); *Sarm*^{GOF} OE wandering (n = 19, 14 animals); *Sarm*^{GOF} OE + *drpr*$^{-/-}$ wandering (n = 10, 6 animals). Freeman-Halton extension of Fisher's exact test.

In image panels above, neurons were labeled by *ppk-MApHS* (A and B) and *ppk>CD4-tdTom* (D-I). C4da-specific KO was induced by *ppk-Cas9*. For all quantifications, **p≤0.01, ***p≤0.001; n.s., not significant. Black bar, mean; red bar, SD. Scale bars, 25 µm.

hrs AEL (Figures 5E, 5G, and 5J). However, *drpr* LOF failed to prevent dendrite fragmentation of Sarm^{GOF} OE neurons at wandering 3rd instar (Figures 5H-5J), suggesting that NAD^+ depletion is able to cause phagocytosis-independent dendrite self-destruction. These results together support the hypothesis that dendrite self-destruction induced by NAD^+ depletion is responsible for fragmentation of injured dendrites when phagocytosis is suppressed.

Injured dendrites undergo severe membrane rupture during dendrite fragmentation

To further understand how injury induces dendrite degeneration, we investigated the extent of membrane rupture during dendrite breakdown using a split GFP-based assay. In this membrane rupture assay (Figure 6A), neurons express myristoylated tdTom-GFP(1-10) and the fat body secretes $GFP(11)_{x7}$ into the hemolymph. $GFP(11)_{x7}$ will bind myr-tdTom-GFP(1-10) and reconstitute fluorescent GFP only when the dendrite membrane is ruptured to allow diffusion of $GFP(11)_{x7}$ into the cytoplasm of neurons. While reconstituted GFP was not detected in uninjured wildtype dendrites (Figure 6 – figure supplement 1A) or degenerating dendrites of *Nmnat* KO neurons (Figure 6B, open arrowheads), it was observed in

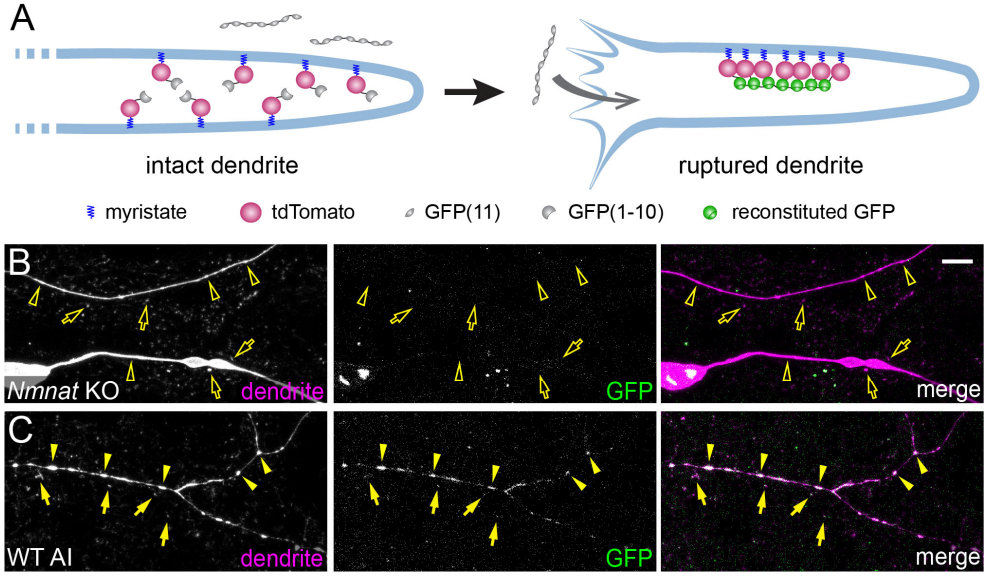

Figure 6. Injured dendrites undergo severe membrane rupture during dendrite fragmentation

(A) A diagram for the membrane rupture assay. Extracellular $GFP(11)_{x7}$ is separated from intracellular myr-tdTom-GFP(1-10) attached to the inner membrane of dendrites. Fluorescent GFP is reconstituted only when the dendrite membrane is ruptured to allow diffusion of $GFP(11)_{x7}$ into the cytoplasm of neurons.

(B) *Nmnat* KO dendrites (open arrowheads) and debris (open arrows) lacking reconstituted GFP in the membrane rupture assay. Scale bar, 25 μm.

(C) Reconstituted GFP labeling of injured wildtype dendrites (arrowheads) and debris (arrows) in the membrane rupture assay. Scale bar, 25 μm. See also Video 3.

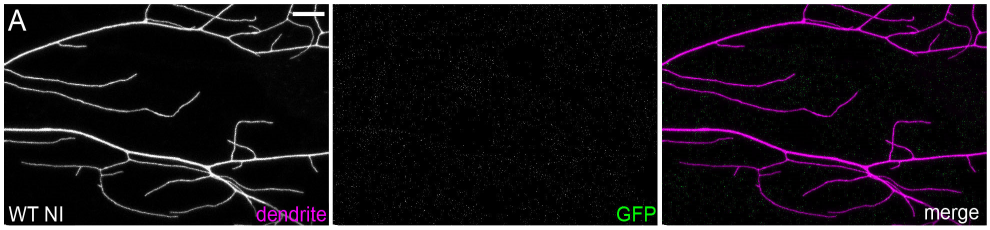

Figure 6 – figure supplement 1. Membrane of uninjured dendrites does not rupture.

(A) Uninjured wildtype dendrites lacking reconstituted GFP in the membrane rupture assay. Scale bar, 25 μm.

severed wildtype dendrites that were undergoing blebbing and fragmentation (Figure 6C, arrowheads), as well as on membrane pieces shed from injured dendrites (Figure 6C, arrows). In time-lapse movies, GFP signals were visible at low levels in injured branches soon after laser ablation, likely due to $GFP(11)_{x7}$ entry through the injury site. The signals were kept at constantly low levels until injured dendrites fragmented, when GFP signals rapidly increased in large dendrite particles (Video 3). These results suggest that injured dendrites undergo severe membrane rupture during fragmentation. In contrast, *Nmnat* KO neurons experience much milder disruptions of membrane integrity, even though they are losing membranes due to the attack of epidermal cells, probably because their dynamically growing branches are efficient in repairing membrane damages.

Calcium flashing precedes PS exposure and fragmentation of injured dendrites

The observed membrane rupture of injured dendrites is consistent with phagocytic attacks of epidermal cells on PS-exposing dendrites. To understand potential signaling events that may lead to dendritic PS exposure and membrane rupture, we examined calcium dynamics in injured dendrites, because calcium influx is essential for and correlates with degeneration of damaged axons in neuronal culture and *in vivo* (George et al., 1995; Williams et al., 2014; Vargas et al., 2015). A previous study in zebrafish identified an initial calcium influx at the time of axon severing and a second calcium wave that coincides with axon fragmentation (Vargas et al., 2015). We recorded calcium dynamics using a membrane-tethered GCaMP6s (myr-GCaMP6s) (Akbergenova et al., 2018), which detected only occasional local rise of calcium in dendrites of wildtype (Video 4) and *Nmnat* KO neurons (Video 5). In the injury model, we observed an initial calcium rise immediately after laser injury in both detached dendrites and the rest of the neurons (Figure 7A, 2s AI). Interestingly, soon after calcium dropped to the baseline level, severed dendrites but not those connected to the cell body entered a phase of continuous calcium flashes that lasted 1-5 hours (Figures 7A at 1h AI, 7D, and Video 6). Afterwards, severed dendrites stayed relatively quiescent for 1-3 hrs before calcium surged again at the time of dendrite blebbing and fragmentation (Figures 7D at 6h AI, 7D and Video 6). All severed dendrites showed flashing, quiescent, and surge phases after injury, even though the exact timing and duration of each phase varied from dendrite to dendrite (Figure 7 – figure supplement 1A).

It was reported that nanoscale ruptures of axonal plasma membrane are responsible for extracellular calcium influx in neuroinflammatory lesions (Witte et al., 2019) and after spinal cord contusion (Williams et al., 2014). To determine whether the last calcium rise that coincides with

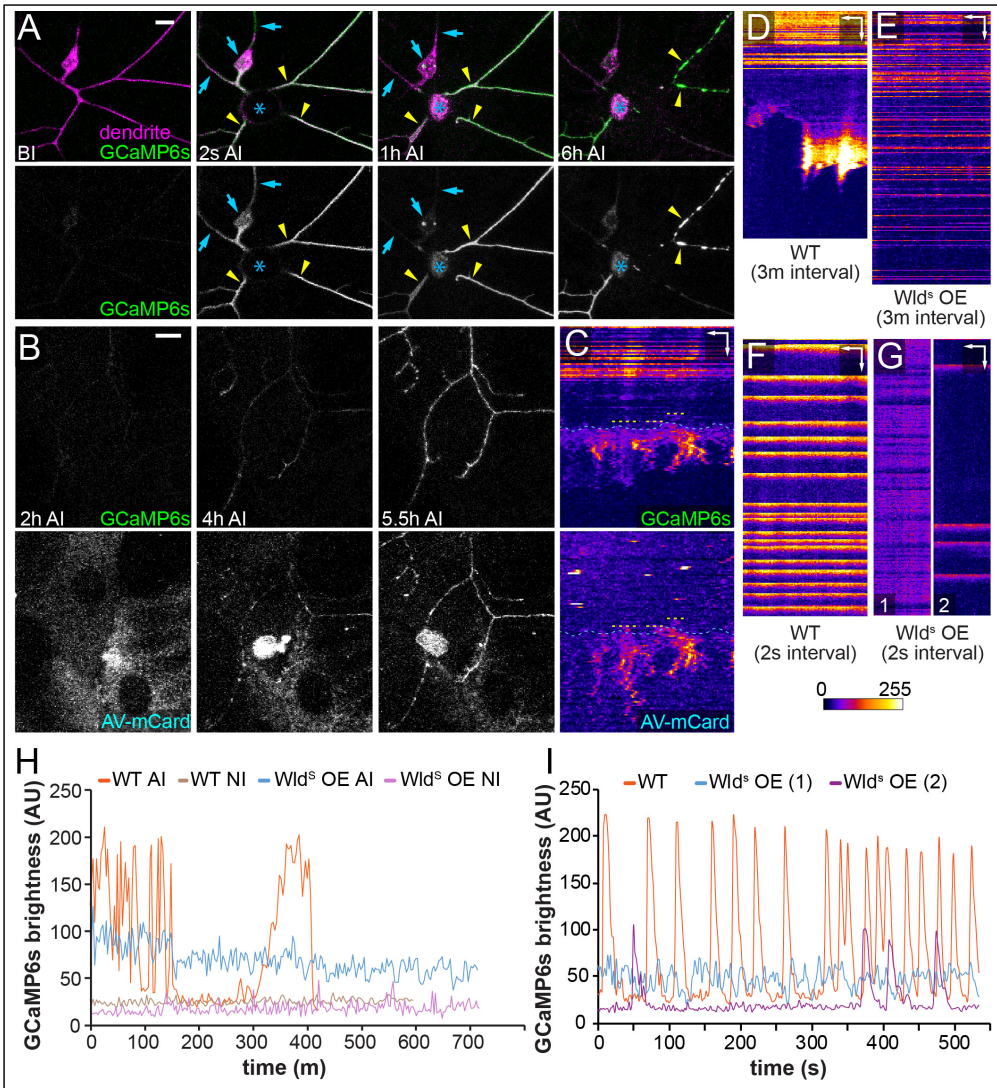

Figure 7. Calcium flashing precedes PS exposure and fragmentation of injured dendrites

(A) A ddaC neuron in a 3rd instar larva expressing myr-GCaMP6s before (BI) and after (2s AI, 1h AI, and 6h AI) laser injury. Blue arrows, uninjured dendrites or cell body; yellow arrowheads, injured dendrites; blue asterisk, injury site. Scale bar, 10 μm. See also Video 6.

(B) Labeling of injured ddaC dendrites expressing GCaMP6s by AV-mCard after (2 h, 4 h, and 5.5 h) injury. Scale bar, 10 μm. See also Video 7.

(C) Kymograph of GCaMP6s signal and AV-mCard binding on an injured dendrite shown in B. Yellow dotted lines, timing of AV-mCard binding; blue dotted lines, timing of the final calcium surge. Scale bars, 3 μm horizontal, 40 min vertical.

(D-E) Kymograph of GCaMP6s signal in wildtype (D) and Wld^S-overexpressing (E) dendrites after injury with 3-min interval. Scale bar, 5 μm horizontal, 60 min vertical. See also Videos 6 and 8.

(F-G) Kymograph of GCaMP6s signal in wildtype (F) and Wld^S-overexpressing (G) dendrites after injury with 2-s interval. See also Videos 9, 10 and 11. Scale bars, 5 μm horizontal, 45 sec vertical.

(H) Plot of GCaMP6s brightness in injured dendrites in (D) and (E) and in uninjured wildtype and Wld^S-overexpressing dendrites over time with 3-min interval. Measurements in injured dendrites start from 0.5-1 hr AI.

(I) Plot of GCaMP6s brightness in injured dendrite in (F) and (G) over time with 2-s interval. Measurements start from 2.5-3 hr AI.

dendrite degeneration could be a result of phagocytosis-induced membrane breakage, we imaged both calcium dynamics and PS exposure of injured dendrites using the PS sensor Annexin V-mCardinal (AV-mCard) (Sapar et al., 2018). AV-mCard labeling of dendrites appeared slightly ahead of the final calcium surge (Figures 7B and 7C, Video 7). Considering that Annexin V-binding to PS and accumulation on dendrite surface are likely slower than calcium activation of GCaMP6s, our data support the idea that PS-mediated phagocytosis causes dendrite membrane rupture and the final calcium surge.

Because the unique pattern of calcium flashing is absent in uninjured dendrites and *Nmnat* KO neurons, we suspected that it may play an active role in promoting degeneration of injured dendrites. If so, factors that can block dendrite degeneration may also alter the calcium flashing. Indeed, Wld^S OE dramatically reduced calcium fluctuations in injured dendrites and eliminated the quiescent and surge phases for the entire duration of our time-lapse imaging (13 hrs) (Figures 7E, 7H, Figure 7 – figure supplement 1B, and Video 8). In addition, using time-lapse imaging at a higher temporal resolution (2 s/frame), we found that wildtype injured dendrites displayed calcium flashes at a frequency of 0.4-3/min (Figures 7F and 7I, and Video 9) while injured dendrites of Wld^S OE neurons either maintained a much milder calcium fluctuation or exhibited irregular and infrequent calcium flashes (Figures 7G and 7I; Videos 10 and 11). These data suggest that high NAD^+ levels suppress calcium flashing in injured dendrites and are consistent with the idea that calcium flashes may promote degeneration of injured dendrites.

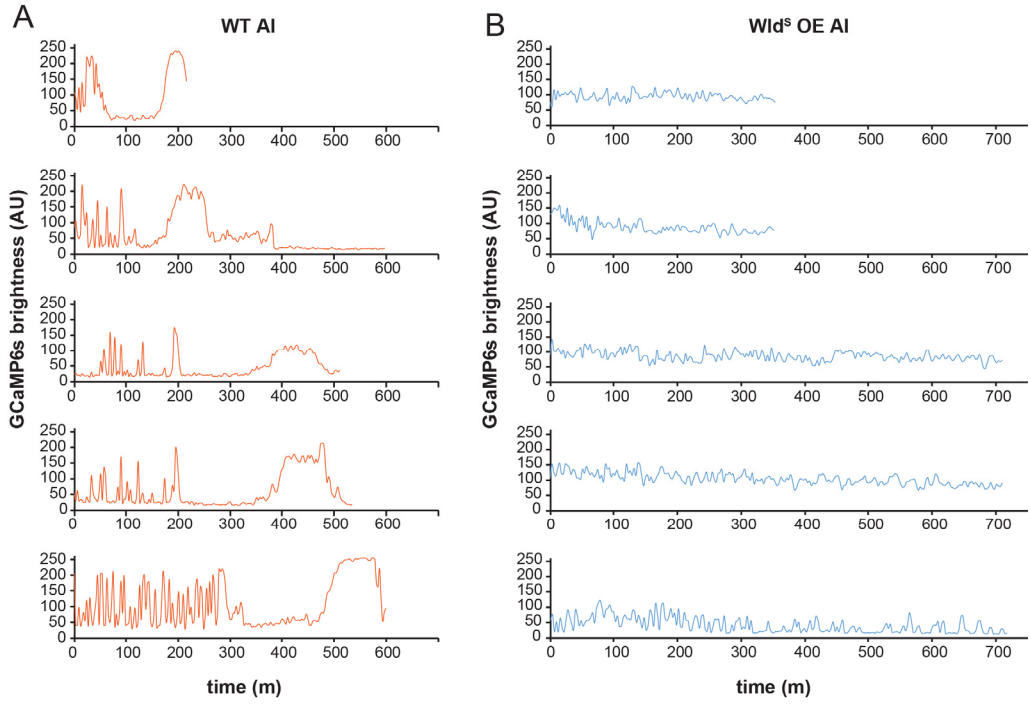

Figure 7 – figure supplement 1. Wld^S overexpression abolished the terminal calcium rise and lowered the amplitude of calcium flashes in injured dendrites.

(A) Representative plots of GCaMP6s brightness in injured wildtype dendrites over time with 3-min interval.

(B) Representative plots of GCaMP6s brightness in injured Wld^S-overexpressing dendrites over time with 3-min interval.

DISCUSSION

In this study, we investigate the contribution of PS-mediated phagocytosis in dendrite degenerations caused by genetic NAD^+ disruptions and injury. Although PS-mediated phagocytosis has been observed after neuronal injury both *in vivo* and *in vitro* (MacDonald et al., 2006; Han et al., 2014; Sapar et al., 2018; Nomura-Komoike et al., 2020), Wallerian degeneration is generally thought as a result of neurite self-destruction triggered by NAD^+ depletion (Babetto et al., 2013; Gerdts et al., 2015; Gerdts et al.,

2016; Neukomm et al., 2017). However, our results strongly suggest that PS exposure-induced phagocytosis is the main driving force for Wallerian degeneration *in vivo*, even though severed neurites can eventually degenerate in the absence of phagocytosis. This conclusion is supported by the observation that ectopic PS exposure on injured dendrites is sufficient to revert the blockage of dendrite fragmentation by Wld^S OE or *Sarm* KO, even though ectopically induced PS exposure is much lower than natural PS exposure on injured dendrites (Sapar et al., 2018). In addition, PS-mediated phagocytosis drives dendrite degeneration induced by genetic reductions of NAD^+: it is solely responsible for dendrite degeneration of *Nmnat* KO neurons and greatly accelerates the degeneration of $Sarm^{GOF}$ OE neurons. Therefore, phagocytosis, rather than neuronal self-destruction, is the main cause of neuronal degeneration related to NAD^+ reduction *in vivo*. Self-destruction is likely a backup mechanism that only takes place when phagocytosis cannot act fast enough to break down neurites. As impairment of NAD^+ metabolism is a general feature of neurodegenerative disorders including Leber congenital amaurosis (LCA), Alzheimer's disease, Parkinson's disease, and retinal degenerations (Ali et al., 2013; Canto et al., 2015; Verdin, 2015; Lin et al., 2016; Fang et al., 2017), phagocytosis may play important roles in the pathogenesis of these diseases through dysregulated neuronal PS exposure.

NAD^+ reduction is known to be essential for neuronal PS exposure and neurite self-destruction during Wallerian degeneration (Gerdts et al., 2015; Sapar et al., 2018; Shacham-Silverberg et al., 2018). How does the same signaling input coordinate the two different events? Our results show that NAD^+ disruption controls PS exposure and neurite self-destruction in separate steps of Wallerian degeneration. In the current model, Sarm activation is believed to cause catastrophic NAD^+ depletion that is sufficient to initiate neurite self-destruction (Gerdts et al., 2015; Sasaki et al., 2016). However, we found that downstream of Sarm activation and before the initiation of self-destruction, neurites first expose PS to engage in phagocytosis-mediated non-autonomous degeneration. Therefore, in our revised model, both intact neurons and severed dendrites respond to at least three distinct, increasingly severe levels of NAD^+ reduction by eliciting different molecular events (Figure 8). Between the NAD^+ level required for Sarm activation (SA level)

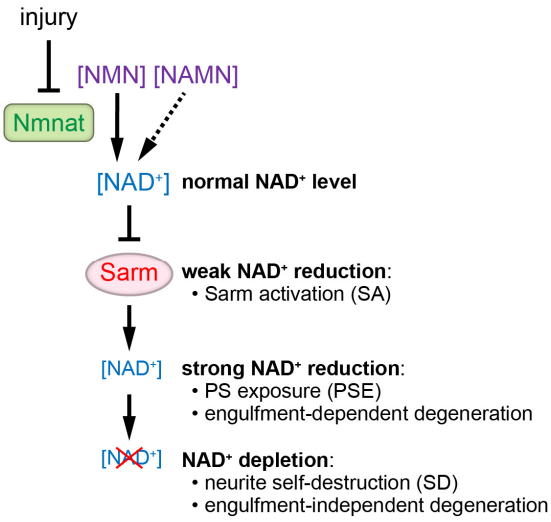

Figure 8. Three levels of NAD^+ reduction elicit distinct responses in dendrites.
See Discussion for details.

and the level that initiates self-destruction (SD level), Sarm activity lowers NAD^+ to a level that causes neurons to expose PS on their surface (which we call the PSE level). This PS exposure causes phagocytosis-mediated dendrite degeneration, which can be completely prevented by blocking engulfment activity of phagocytes. However, below the SD level, neurites spontaneously fragment even in the absence of phagocytosis.

Our results also suggest a direct correlation between the kinetics of NAD^+ reduction and the severity of neurite degeneration. *Nmnat* KO is expected to cause slow NAD^+ reduction, due to gene perdurance and the time required for natural NAD^+ turnover, and correspondingly causes engulfment-dependent dendrite degeneration only in late 3rd instar larvae. In contrast, $Sarm^{GOF}$ OE should lead to a more rapid NAD^+ depletion and in fact causes engulfment-dependent dendrite degeneration as early as the 1st instar and dendrite self-destruction by the 3rd instar. Injury apparently causes even more rapid NAD^+ reduction in axons (Wang et al., 2005) and is correlated with the fastest dendrite degeneration – initiation at around 4 hrs AI and completion usually by 10 hrs AI.

How does NAD^+ reduction cause PS exposure? A direct consequence of NAD^+ loss is decline of neurite ATP levels due to the requirement of NAD^+ in glycolysis and oxidative phosphorylation (Wang et al., 2005; Shacham-Silverberg et al., 2018). Consistent with ATP reduction playing a role in inducing PS exposure, suppressing mitochondria ATP synthesis in DRG culture caused gradual axonal PS exposure (Shacham-Silverberg et al., 2018). However, how ATP reduction may induce PS exposure remain elusive. Although the maintenance of membrane PS asymmetry by flippases requires ATP, flippase KO in C4da neurons causes a much milder PS exposure than injury (Sapar et al., 2018), suggesting that mechanisms other than flippase inhibition must be contributing to the rapid PS exposure seen after injury. Identifying the PS transporters responsible for PS exposure on injured neurites will be a key step for revealing the mechanisms of NAD^+ regulation of PS exposure.

By exploring the different mechanisms employed in *Nmnat* KO- and injury-induced dendrite degenerations, we discovered dynamic calcium activities only present in injured dendrites, including an unreported calcium flashing pattern prior to any obvious degenerative event and a final calcium surge that coincides with dendrite fragmentation. Calcium surge at the time of neurite fragmentation is a shared feature between injured axons of zebrafish (Vargas et al., 2015) and injured dendrites of *Drosophila* da neurons. Although calcium influx is required for Wallerian degeneration (George et al., 1995) and may activate calcium-dependent lipid scramblases (Suzuki et al., 2010), our time-lapse

analyses suggest that the final calcium surge is more likely a result of phagocytosis-induced membrane rupture rather than the cause of fragmentation. In comparison, the calcium flashing soon after the injury may play an active role in dendrite degeneration in ways similar to the compartmentalized calcium flashing that occurs during developmental pruning of C4da neurons (Kanamori et al., 2013). Consistent with this possibility, the calcium flashing is suppressed by elevating NAD^+ level through Wld^S OE. It remains to be determined if the calcium flashing contribute to the induction of PS exposure, or dendrite self-destruction, or both by accelerating NAD^+ consumption.

Lastly, a surprising finding of our study is that at least in sensory dendrites, components of the Wallerian degeneration pathway, including Axed, Peb, and JNK signaling, do not appear to be involved in neuronal PS exposure or dendrite self-destruction, even though they have been implicated in injury-induced axon degeneration in other contexts. Therefore, our results suggest that NAD^+ disruption is likely the only shared mechanism of neurite breakdown in Wallerian degeneration.

METHODS

Fly strains

The details of fly strains used in this study are listed in the key reagent table. For labeling of C4da neurons, we used *ppk-CD4-tdTom*, *ppk-MApHS*, and *ppk-Gal4 UAS-CD4-tdTom*. For labeling PS exposure on dendrites, we used *dcg-Gal4 UAS-GFP-LactC1C2*, *R16A03-LexA LexAop-GFP-LactC1C2*, and *dcg-Gal4 UAS-AnnexinV-mCard*. To label Or22a axons, we used *Or22a-Gal4 UAS-mCD8-GFP*. To visualize dendrite rupture, we used *dcg-Gal4 UAS-sGFP(11)x7* together with *ppk-LexA LexAop-myr-tdTom-GFP(1-10)*. To visualize calcium activities in C4da dendrites, we used *ppk-LexA LexAop-myr-GCaMP6s*.

Molecular cloning and transgenic flies

ey-Cas9: Three tandem copies of a 211bp *ey* enhancer (corresponding to nucleotides 2577-2787 in GenBank accession number AJ131630) was inserted into XhoI/SalI sites of pENTR11 (Thermo Fisher Scientific). The resulting entry vector was combined with a Cas9 destination vector which is similar to pDEST-APIC-Cas9 (Addgene 121657) but does not contain Inr, MTE, and DPE in the Hsp70 core promoter (Poe et al., 2019) to generate the pAPIC-ey-Cas9 expression vector through a Gateway LR reaction.

LexAop-myr-tdTom-GFP(1-10): pAPLO-CD4-tdTom (Poe et al., 2017) was digested by BglII/AscI, blunted, and religated to remove an XbaI site before 13xLexAop2. The resulting construct is called pAPLOm-CD4-tdTom. An myr-GFP fragment was isolated from pJFRC176-10XUAS-rox-dSTOP-rox-myr-GFP (Addgene 32147) by XhoI/XbaI digestion and ligated to XhoI/XbaI sites of pAPLOm-CD4-tdTom to make pAPLO-myr-GFP. pAPLO-myr-GFP was then digested by BamHI/XbaI and subsequently assembled with a tdTom PCR fragment and a GFP(1-10) gBlock fragment (synthesized by IDT) through NEBuilder DNA Assembly to generate pAPLO-myr-tdTom-GFP1-10.

UAS-sGFP(11)x7: A DNA fragment containing GFP(11)x7 was PCR amplified from a gBlock DNA fragment and cloned into Nhe/XbaI sites of pIHEU-sfGFP-LactC1C2 using NEBuilder DNA Assembly. The resulting construct pIHEU-sGFP11x7 inherits the signal peptide sequence from pIHEU-sfGFP-LactC1C2 but removes the sfGFP-LactC1C2 coding sequence.

LexAop-WldS: The WldS coding sequence was PCR amplified from UAS-WldS genomic DNA and cloned into XhoI/XbaI sites of pAPLOm-CD4-tdTom via restriction cloning to make pAPLO-WldS.

gRNA expression vectors: For *Nmnat*, *Sarm*, and *axed*, gRNAs were cloned into pAC-U63-tgRNA-Rev as described (Poe et al., 2019). The 2nd tRNA in each final construct is glutamine tRNA instead of glycine tRNA. For *peb*, the gRNA vector is similar to pAC-U63-tgRNA-Rev but contains a modified gRNA scaffold, a TagBFP driven by a Ubi-p63E promoter, and a gRNA targeting TagBFP. This gRNA vector will be published elsewhere. Each of the final gRNA constructs contains two gRNA target sequences as listed in the table below.

Gene	Target sequence 1	Target sequence 2
Sarm	GCATCTGTTCAAACACTCCG	CGATTCCAATATCAGCCCGG
Nmnat	GGAACCCACAGAGTGGTAGG	TAAGAGCCGCCGAATCAACG
axed	GTCGGTACTCGAGCGGAGCG	TGGACCCGATGGCCATCACG
peb	ATTTCGTCTGAATCGCTCGG	ACGCATGTGACGCACCAGGG

The above constructs were injected by Rainbow Transgenic Flies to transform flies through φC31 integrase-mediated integration into attP docker sites. The sequences of constructs will be provided upon request.

CRISPR-TRiM

The efficiency of transgenic gRNA lines was validated by the Cas9-LEThAL assay (Poe et al., 2019). Homozygous males of each gRNA line were crossed to *Act-Cas9 w lig4* homozygous females. *gRNA-Nmnat* crosses caused lethality of all progeny at the 2nd instar larval stage; *gRNA-Sarm* crosses yielded viable female progeny and male lethality between 3rd instar larvae to prepupae; *gRNA-axed* crosses caused lethality at the embryonic stage for all progeny; *gRNA-peb* crosses caused lethality from embryonic stage to the 2nd instar for all progeny. These results suggest that all gRNAs are efficient.

C4da-specific gene knockout was carried out using *ppk-Cas9* (Poe et al., 2019). Tissue-specific knockout in da neuron precursor cells were carried out with *SOP-Cas9* (Poe et al., 2019). Gene knockout in the precursor cells of Or22a ORNs was carried out using *ey-Cas9* (this study).

Live imaging

Animals were reared at 25°C in density-controlled vials (60-100 embryos/vial) on standard yeast-glucose medium (doi:10.1101/pdb.rec10907). Larvae at 125 hours AEL (wandering stage) or stages specified were mounted in 100% glycerol under coverslips with vacuum grease spacer and imaged using a Leica SP8 microscope equipped with a 40X NA1.30 oil objective. Larvae were lightly anesthetized with isoflurane before mounting. For consistency, we imaged dorsal ddaC neurons from A1-A3 segments (2-3 neurons per animal) on one side of the larvae. Unless stated otherwise, confocal images shown in all figures are maximum intensity projections of z stacks encompassing the epidermal layer and the sensory neurons beneath, which are typically 8–10 μm for 3rd instar larvae.

Injury assay

Injury assay at the larval stage was done as described previously (Sapar et al., 2018). Briefly, larvae at 90 hr AEL were lightly anesthetized with isoflurane, mounted in a small amount of halocarbon oil under coverslips with grease spacers. The laser ablation was performed on a Zeiss LSM880 Confocal/Multiphoton Upright Microscope, using a 790 nm two-photon laser at primary dendrites of ddaC neurons in A1 and A3 segments. Animals were recovered on grape juice agar plates following lesion for appropriate times before imaging.

ORN axon injury assay was performed on 7-day-old male flies by removing the outer segments of both antennae as described in (MacDonald et al., 2006). The injured males were recovered for 7 days by transferring to fresh yeast-glucose medium every day. To examine Or22a axon degeneration, brains were dissected in PBST (0.2% Triton-X in PBS), fixed in 4% formaldehyde in PBS for 20 min, and then

rinsed with PBST three times, 20 minutes each. Then the brains were mounted in SlowFade® Diamond Antifade Mountant (Thermo Fisher Scientific) and imaged using a Leica SP8 microscope with a 40x NA1.3 oil objective.

Long-term time-lapse imaging

Long-term time-lapse imaging at the larval stage was done as described previously (Sapar et al., 2018; Ji and Han, 2020). Briefly, a layer of double-sided tape was placed on the coverslip to define the position of PDMS blocks. A small amount of UV glue was added to the groove of PDMS and to the coverslip. Anesthetized larvae were placed on top of the UV glue on the coverslip and then covered by PDMS blocks with the groove side contacting the larva. Glue was then cured by 365nm UV light. The coverslip with attached PDMS and larvae was mounted on an aluminum slide chamber that contained a piece of moisturized Kimwipes (Kimtech Science) paper. Time-lapse imaging was performed on a Leica SP8 confocal equipped with a 40x NA1.3 oil objective and a resonant scanner at digital zoom 0.75 and a 3-min or 2-sec interval. For imaging after ablation, larvae were pre-mounted in the imaging chamber and subjected to laser injury. The larvae were then imaged 0.5-1 hours after ablation. For calcium imaging before and immediately after ablation, images were captured on a Zeiss LSM880 Confocal/Multiphoton Upright Microscope on which the ablation was performed.

Image analysis and quantification

Image processing and analyses were done in Fiji/ImageJ. Methods for tracing and measuring C4da neuron dendrite length have been previously described (Poe et al., 2017). Briefly, the images were segmented by Auto Local Threshold and reduced to single pixel skeletons before measurement of skeleton length by pixel distance. The dendrite debris measurement has been described previously (Sapar et al., 2018). Briefly, a dendrite mask was first generated from projected images by Auto Local Threshold in order to create a region of interest (ROI) by dilation to map areas within one-epidermal-cell diameter (40 μm) from dendrites. Dendrite debris within the ROI was converted to binary masks based on fixed thresholds. Different thresholds were used for *ppk-C4-tdTom* and *ppk-Gal4 UAS-CD-tdTom* as they have different brightness. The dendrite pixel area (ADen), debris pixel area (ADeb), and ROI area (AROI) were measured and dendrite coverage ratio was calculated based on the following formula: $100 \cdot Adeb \cdot AROI / (AROI - ADen) \cdot ADen$. For measuring Lact-GFP, two regions at empty epidermal regions were measured as background levels. TdTom signals on dendrites were used to generate dendrite masks for measurement of GFP within the masks. For kymographs, we used a custom macro

based on the Straighten function to extract a strip of pixels centered at the selected dendrite branch. The maximum intensity pixel in the strip at each distance was used to generate a single-pixel line for each time frame. The final kymographs were displayed using the Fire lookup table (LUT).

Statistical Analysis

R was used to conduct statistical analyses and generate graphs. (*$p < 0.05$, **$p < 0.01$, and ***$p < 0.001$). Statistical significance was set at $p < 0.05$. Data acquisition and quantification were performed non-blinded. Acquisition was performed in ImageJ (batch processing for debris coverage ratio and fragmentation ratio, manually by hand for GFP-Lact binding) and Microsoft Excel. Statistical analyses were performed using R. We used the following R packages: car, stats, multcomp for statistical analysis and ggplot2 for generating graphs. Some graphs were made in Excel using its native plotting functions. For the statistical analysis we ran the following tests, ANOVA (followed by Tukey's HSD) when dependent variable was normally distributed and there was approximately equal variance across groups. When dependent variable was not normally distributed and variance was not equal across groups, we used Kruskal-Wallis (followed by Dunn's test, p-values adjusted with Benjamini-Hochberg method) to test the null hypothesis that assumes that the samples (groups) are from identical populations. To check whether the data fit a normal distribution, we generated qqPlots to analyze whether the residuals of the linear regression model is normally distributed. We used the Levene's test to check for equal variance within groups. The state of neuronal degeneration caused by $Sarm^{GOF}$ OE was compared using the Freeman-Halton extension of Fisher's exact test (https://www.danielsoper.com/statcalc/calculator.aspx?id=58).

Replication

For all larval and adult imaging experiments, at least 3 biological replications were performed for each genotype and/or condition.

AUTHOR CONTRIBUTIONS

Conceptualization, CH, MLS, AS, HJ; Methodology, CH, MLS, AS, HJ, BW; Investigation, MLS, AS, HJ; Formal Analysis, MLS, AS, HJ; Resources, CH, MLS, AS, HJ, BW; Writing – Original Draft, CH, MLS, AS, HJ; Writing – Review and Editing, CH, MLS, AS, HJ; Funding Acquisition, CH.

ACKNOWLEDGMENTS

We thank Marc Freeman, Yang Xiang, Heather Broihier, and Bloomington Stock Center for fly stocks; Addgene for plasmids; Cornell BRC Imaging facility for access to microscopes (funded by NIH grant S10OD018516); Cornell CSCU for advice on statistics; Mike Goldberg and Fenghua Hu for critical reading and suggestions on the manuscript. This work was supported by a Cornell start-up fund and NIH grants (R01NS099125 and R21OD023824) awarded to C.H.

DECLARATION OF INTEREST

The authors declare no competing interests.

REFERENCE

Akbergenova, Y., Cunningham, K.L., Zhang, Y.V., Weiss, S., and Littleton, J.T., 2018. Characterization of developmental and molecular factors underlying release heterogeneity at Drosophila synapses. Elife *7*. https://doi.org/10.7554/eLife.38268.

Ali, Y.O., Li-Kroeger, D., Bellen, H.J., Zhai, R.G., and Lu, H.C., 2013. NMNATs, evolutionarily conserved neuronal maintenance factors. Trends Neurosci *36*, 632-640. https://doi.org/10.1016/j.tins.2013.07.002.

Avery, M.A., Sheehan, A.E., Kerr, K.S., Wang, J., and Freeman, M.R., 2009. Wld S requires Nmnat1 enzymatic activity and N16-VCP interactions to suppress Wallerian degeneration. J Cell Biol *184*, 501-513. https://doi.org/10.1083/jcb.200808042.

Babetto, E., Beirowski, B., Russler, E.V., Milbrandt, J., and DiAntonio, A., 2013. The Phr1 ubiquitin ligase promotes injury-induced axon self-destruction. Cell Rep *3*, 1422-1429. https://doi.org/10.1016/j.celrep.2013.04.013.

Canto, C., Menzies, K.J., and Auwerx, J., 2015. NAD(+) Metabolism and the Control of Energy Homeostasis: A Balancing Act between Mitochondria and the Nucleus. Cell Metab *22*, 31-53. https://doi.org/10.1016/j.cmet.2015.05.023.

Coleman, M.P., and Freeman, M.R., 2010. Wallerian degeneration, wld(s), and nmnat. Annu Rev Neurosci *33*, 245-267. https://doi.org/10.1146/annurev-neuro-060909-153248.

Collins, C.A., Wairkar, Y.P., Johnson, S.L., and DiAntonio, A., 2006. Highwire restrains synaptic growth by attenuating a MAP kinase signal. Neuron *51*, 57-69. https://doi.org/10.1016/j.neuron.2006.05.026.

553 Davies, A.J., Kim, H.W., Gonzalez-Cano, R., Choi, J., Back, S.K., Roh, S.E., Johnson, E., Gabriac, M.,
554 Kim, M.S., Lee, J.*, et al.*, 2019. Natural Killer Cells Degenerate Intact Sensory Afferents following
555 Nerve Injury. Cell *176*, 716-728 e718. https://doi.org/10.1016/j.cell.2018.12.022.

556 Di Stefano, M., Nascimento-Ferreira, I., Orsomando, G., Mori, V., Gilley, J., Brown, R., Janeckova, L.,
557 Vargas, M.E., Worrell, L.A., Loreto, A.*, et al.*, 2015. A rise in NAD precursor nicotinamide
558 mononucleotide (NMN) after injury promotes axon degeneration. Cell Death Differ *22*, 731-742.
559 https://doi.org/10.1038/cdd.2014.164.

560 Fang, E.F., Lautrup, S., Hou, Y., Demarest, T.G., Croteau, D.L., Mattson, M.P., and Bohr, V.A., 2017.
561 NAD(+) in Aging: Molecular Mechanisms and Translational Implications. Trends Mol Med *23*, 899-
562 916. https://doi.org/10.1016/j.molmed.2017.08.001.

563 Farley, J.E., Burdett, T.C., Barria, R., Neukomm, L.J., Kenna, K.P., Landers, J.E., and Freeman, M.R.,
564 2018. Transcription factor Pebbled/RREB1 regulates injury-induced axon degeneration. Proc Natl Acad
565 Sci U S A *115*, 1358-1363. https://doi.org/10.1073/pnas.1715837115.

566 Fourgeaud, L., Traves, P.G., Tufail, Y., Leal-Bailey, H., Lew, E.D., Burrola, P.G., Callaway, P.,
567 Zagorska, A., Rothlin, C.V., Nimmerjahn, A.*, et al.*, 2016. TAM receptors regulate multiple features of
568 microglial physiology. Nature *532*, 240-244. https://doi.org/10.1038/nature17630.

569 Freeman, M.R., Delrow, J., Kim, J., Johnson, E., and Doe, C.Q., 2003. Unwrapping glial biology: Gcm
570 target genes regulating glial development, diversification, and function. Neuron *38*, 567-580.
571 https://doi.org/10.1016/s0896-6273(03)00289-7.

572 Galloway, D.A., Phillips, A.E.M., Owen, D.R.J., and Moore, C.S., 2019. Phagocytosis in the Brain:
573 Homeostasis and Disease. Front Immunol *10*, 790. https://doi.org/10.3389/fimmu.2019.00790.

574 George, E., Glass, J., and Griffin, J., 1995. Axotomy-induced axonal degeneration is mediated by
575 calcium influx through ion-specific channels. The Journal of Neuroscience *15*, 6445-6452.
576 https://doi.org/10.1523/jneurosci.15-10-06445.1995.

577 Gerdts, J., Brace, E.J., Sasaki, Y., DiAntonio, A., and Milbrandt, J., 2015. SARM1 activation triggers
578 axon degeneration locally via NAD(+) destruction. Science *348*, 453-457.
579 https://doi.org/10.1126/science.1258366.

Gerdts, J., Summers, D.W., Milbrandt, J., and DiAntonio, A., 2016. Axon Self-Destruction: New Links among SARM1, MAPKs, and NAD+ Metabolism. Neuron *89*, 449-460. https://doi.org/10.1016/j.neuron.2015.12.023.

Han, C., Jan, L.Y., and Jan, Y.N., 2011. Enhancer-driven membrane markers for analysis of nonautonomous mechanisms reveal neuron-glia interactions in Drosophila. Proc Natl Acad Sci U S A *108*, 9673-9678. https://doi.org/10.1073/pnas.1106386108.

Han, C., Song, Y., Xiao, H., Wang, D., Franc, N.C., Jan, L.Y., and Jan, Y.N., 2014. Epidermal cells are the primary phagocytes in the fragmentation and clearance of degenerating dendrites in Drosophila. Neuron *81*, 544-560. https://doi.org/10.1016/j.neuron.2013.11.021.

Ji, H., and Han, C., 2020. LarvaSPA, A Method for Mounting Drosophila Larva for Long-Term Time-Lapse Imaging. J Vis Exp. https://doi.org/10.3791/60792.

Kanamori, T., Kanai, M.I., Dairyo, Y., Yasunaga, K., Morikawa, R.K., and Emoto, K., 2013. Compartmentalized calcium transients trigger dendrite pruning in Drosophila sensory neurons. Science *340*, 1475-1478. https://doi.org/10.1126/science.1234879.

Leventis, P.A., and Grinstein, S., 2010. The distribution and function of phosphatidylserine in cellular membranes. Annu Rev Biophys *39*, 407-427. https://doi.org/10.1146/annurev.biophys.093008.131234.

Lin, J.B., Kubota, S., Ban, N., Yoshida, M., Santeford, A., Sene, A., Nakamura, R., Zapata, N., Kubota, M., Tsubota, K.*, et al.*, 2016. NAMPT-Mediated NAD(+) Biosynthesis Is Essential for Vision In Mice. Cell Rep *17*, 69-85. https://doi.org/10.1016/j.celrep.2016.08.073.

Liu, H.W., Smith, C.B., Schmidt, M.S., Cambronne, X.A., Cohen, M.S., Migaud, M.E., Brenner, C., and Goodman, R.H., 2018. Pharmacological bypass of NAD(+) salvage pathway protects neurons from chemotherapy-induced degeneration. Proc Natl Acad Sci U S A. https://doi.org/10.1073/pnas.1809392115.

MacDonald, J.M., Beach, M.G., Porpiglia, E., Sheehan, A.E., Watts, R.J., and Freeman, M.R., 2006. The Drosophila cell corpse engulfment receptor Draper mediates glial clearance of severed axons. Neuron *50*, 869-881. https://doi.org/10.1016/j.neuron.2006.04.028.

Mack, T.G., Reiner, M., Beirowski, B., Mi, W., Emanuelli, M., Wagner, D., Thomson, D., Gillingwater, T., Court, F., Conforti, L.*, et al.*, 2001. Wallerian degeneration of injured axons and synapses is delayed by a Ube4b/Nmnat chimeric gene. Nat Neurosci *4*, 1199-1206. https://doi.org/10.1038/nn770.

609 Mazaheri, F., Breus, O., Durdu, S., Haas, P., Wittbrodt, J., Gilmour, D., and Peri, F., 2014. Distinct roles
610 for BAI1 and TIM-4 in the engulfment of dying neurons by microglia. Nat Commun *5*, 4046.
611 https://doi.org/10.1038/ncomms5046.

612 Miller, B.R., Press, C., Daniels, R.W., Sasaki, Y., Milbrandt, J., and DiAntonio, A., 2009. A dual
613 leucine kinase-dependent axon self-destruction program promotes Wallerian degeneration. Nat Neurosci
614 *12*, 387-389. https://doi.org/10.1038/nn.2290.

615 Nandrot, E.F., Anand, M., Almeida, D., Atabai, K., Sheppard, D., and Finnemann, S.C., 2007. Essential
616 role for MFG-E8 as ligand for alphavbeta5 integrin in diurnal retinal phagocytosis. Proc Natl Acad Sci
617 U S A *104*, 12005-12010. https://doi.org/10.1073/pnas.0704756104.

618 Neukomm, L.J., Burdett, T.C., Gonzalez, M.A., Zuchner, S., and Freeman, M.R., 2014. Rapid in vivo
619 forward genetic approach for identifying axon death genes in Drosophila. Proc Natl Acad Sci U S A
620 *111*, 9965-9970. https://doi.org/10.1073/pnas.1406230111.

621 Neukomm, L.J., Burdett, T.C., Seeds, A.M., Hampel, S., Coutinho-Budd, J.C., Farley, J.E., Wong, J.,
622 Karadeniz, Y.B., Osterloh, J.M., Sheehan, A.E.*, et al.*, 2017. Axon Death Pathways Converge on
623 Axundead to Promote Functional and Structural Axon Disassembly. Neuron *95*, 78-91 e75.
624 https://doi.org/10.1016/j.neuron.2017.06.031.

625 Nomura-Komoike, K., Saitoh, F., and Fujieda, H., 2020. Phosphatidylserine recognition and Rac1
626 activation are required for Muller glia proliferation, gliosis and phagocytosis after retinal injury. Sci Rep
627 *10*, 1488. https://doi.org/10.1038/s41598-020-58424-6.

628 Osterloh, J.M., Yang, J., Rooney, T.M., Fox, A.N., Adalbert, R., Powell, E.H., Sheehan, A.E., Avery,
629 M.A., Hackett, R., Logan, M.A.*, et al.*, 2012. dSarm/Sarm1 is required for activation of an injury-
630 induced axon death pathway. Science *337*, 481-484. https://doi.org/10.1126/science.1223899.

631 Poe, A.R., Tang, L., Wang, B., Li, Y., Sapar, M.L., and Han, C., 2017. Dendritic space-filling requires a
632 neuronal type-specific extracellular permissive signal in Drosophila. Proc Natl Acad Sci U S A *114*,
633 E8062-E8071. https://doi.org/10.1073/pnas.1707467114.

634 Poe, A.R., Wang, B., Sapar, M.L., Ji, H., Li, K., Onabajo, T., Fazliyeva, R., Gibbs, M., Qiu, Y., Hu, Y.*,*
635 *et al.*, 2019. Robust CRISPR/Cas9-Mediated Tissue-Specific Mutagenesis Reveals Gene Redundancy
636 and Perdurance in Drosophila. Genetics *211*, 459-472. https://doi.org/10.1534/genetics.118.301736.

637 Sapar, M.L., and Han, C., 2019. Die in pieces: How Drosophila sheds light on neurite degeneration and
638 clearance. J Genet Genomics *46*, 187-199. https://doi.org/10.1016/j.jgg.2019.03.010.

639 Sapar, M.L., Ji, H., Wang, B., Poe, A.R., Dubey, K., Ren, X., Ni, J.Q., and Han, C., 2018.
640 Phosphatidylserine Externalization Results from and Causes Neurite Degeneration in Drosophila. Cell
641 Rep *24*, 2273-2286. https://doi.org/10.1016/j.celrep.2018.07.095.

642 Sasaki, Y., Nakagawa, T., Mao, X., DiAntonio, A., and Milbrandt, J., 2016. NMNAT1 inhibits axon
643 degeneration via blockade of SARM1-mediated NAD(+) depletion. Elife *5*.
644 https://doi.org/10.7554/eLife.19749.

645 Segawa, K., Suzuki, J., and Nagata, S., 2011. Constitutive exposure of phosphatidylserine on viable
646 cells. Proc Natl Acad Sci U S A *108*, 19246-19251. https://doi.org/10.1073/pnas.1114799108.

647 Shacham-Silverberg, V., Sar Shalom, H., Goldner, R., Golan-Vaishenker, Y., Gurwicz, N., Gokhman, I.,
648 and Yaron, A., 2018. Phosphatidylserine is a marker for axonal debris engulfment but its exposure can
649 be decoupled from degeneration. Cell Death Dis *9*, 1116. https://doi.org/10.1038/s41419-018-1155-z.

650 Suzuki, J., Umeda, M., Sims, P.J., and Nagata, S., 2010. Calcium-dependent phospholipid scrambling by
651 TMEM16F. Nature *468*, 834-838. https://doi.org/10.1038/nature09583.

652 Tanaka, K., Fujimura-Kamada, K., and Yamamoto, T., 2011. Functions of phospholipid flippases. J
653 Biochem *149*, 131-143. https://doi.org/10.1093/jb/mvq140.

654 Tao, J., and Rolls, M.M., 2011. Dendrites have a rapid program of injury-induced degeneration that is
655 molecularly distinct from developmental pruning. J Neurosci *31*, 5398-5405.
656 https://doi.org/10.1523/JNEUROSCI.3826-10.2011.

657 Tung, T.T., Nagaosa, K., Fujita, Y., Kita, A., Mori, H., Okada, R., Nonaka, S., and Nakanishi, Y., 2013.
658 Phosphatidylserine recognition and induction of apoptotic cell clearance by Drosophila engulfment
659 receptor Draper. J Biochem *153*, 483-491. https://doi.org/10.1093/jb/mvt014.

660 Vargas, M.E., Yamagishi, Y., Tessier-Lavigne, M., and Sagasti, A., 2015. Live Imaging of Calcium
661 Dynamics during Axon Degeneration Reveals Two Functionally Distinct Phases of Calcium Influx. J
662 Neurosci *35*, 15026-15038. https://doi.org/10.1523/JNEUROSCI.2484-15.2015.

663 Verdin, E., 2015. NAD(+) in aging, metabolism, and neurodegeneration. Science *350*, 1208-1213.
664 https://doi.org/10.1126/science.aac4854.

Waller, A., 1850. Experiments on the Section of the Glossopharyngeal and Hypoglossal Nerves of the Frog, and Observations of the Alterations Produced Thereby in the Structure of Their Primitive Fibres. Philosophical Transactions of the Royal Society of London *140*, 423-429.

Wang, J., Zhai, Q., Chen, Y., Lin, E., Gu, W., McBurney, M.W., and He, Z., 2005. A local mechanism mediates NAD-dependent protection of axon degeneration. J Cell Biol *170*, 349-355. https://doi.org/10.1083/jcb.200504028.

Wen, Y., Parrish, J.Z., He, R., Zhai, R.G., and Kim, M.D., 2011. Nmnat exerts neuroprotective effects in dendrites and axons. Mol Cell Neurosci *48*, 1-8. https://doi.org/10.1016/j.mcn.2011.05.002.

Williams, P.R., Marincu, B.N., Sorbara, C.D., Mahler, C.F., Schumacher, A.M., Griesbeck, O., Kerschensteiner, M., and Misgeld, T., 2014. A recoverable state of axon injury persists for hours after spinal cord contusion in vivo. Nat Commun *5*, 5683. https://doi.org/10.1038/ncomms6683.

Witte, M.E., Schumacher, A.M., Mahler, C.F., Bewersdorf, J.P., Lehmitz, J., Scheiter, A., Sanchez, P., Williams, P.R., Griesbeck, O., Naumann, R.*, et al.*, 2019. Calcium Influx through Plasma-Membrane Nanoruptures Drives Axon Degeneration in a Model of Multiple Sclerosis. Neuron *101*, 615-624 e615. https://doi.org/10.1016/j.neuron.2018.12.023.

Xiong, X., Hao, Y., Sun, K., Li, J., Li, X., Mishra, B., Soppina, P., Wu, C., Hume, R.I., and Collins, C.A., 2012. The Highwire ubiquitin ligase promotes axonal degeneration by tuning levels of Nmnat protein. PLoS Biol *10*, e1001440. https://doi.org/10.1371/journal.pbio.1001440.

Yang, J., Wu, Z., Renier, N., Simon, D.J., Uryu, K., Park, D.S., Greer, P.A., Tournier, C., Davis, R.J., and Tessier-Lavigne, M., 2015. Pathological axonal death through a MAPK cascade that triggers a local energy deficit. Cell *160*, 161-176. https://doi.org/10.1016/j.cell.2014.11.053.

Zhai, R.G., Cao, Y., Hiesinger, P.R., Zhou, Y., Mehta, S.Q., Schulze, K.L., Verstreken, P., and Bellen, H.J., 2006. Drosophila NMNAT maintains neural integrity independent of its NAD synthesis activity. PLoS Biol *4*, e416. https://doi.org/10.1371/journal.pbio.0040416.

Zhai, R.G., Rizzi, M., and Garavaglia, S., 2009. Nicotinamide/nicotinic acid mononucleotide adenylyltransferase, new insights into an ancient enzyme. Cell Mol Life Sci *66*, 2805-2818. https://doi.org/10.1007/s00018-009-0047-x.

VIDEO LEGEND

Video 1. GFP-Lact labeling of degenerating *Nmnat* KO dendrites, related to Figure 2.

Time-lapse movie of GFP-Lact labeling on distal dendrites of a *Nmnat* KO C4da neuron before and during degeneration. Imaging started around 96 hours AEL. *Dcg-Gal4* drives GFP-Lact expression in both fat bodies (not shown) and hemocytes (mobile cells in the GFP-Lact channel). Timestamp is relative to the first frame, with a 3-min interval between each frame.

Video 2. Dendrite dynamics of *Nmnat* KO neurons in *drpr* mutant larvae, related to Figure 2.

Time-lapse movie of dendrites of a *Nmnat* KO neuron exhibiting dynamic extension and retraction behaviors in a *drpr* mutant larva. Imaging started around 120 hours AEL. Timestamp is relative to the first frame, with a 3-min interval between each frame.

Video 3. Membrane rupture of injured dendrites, related to Figure 6.

Time-lapse movie of laser-injured C4da dendrites from 1 to 11 hours AI. Reconstituted GFP is from extracellular $GFP(11)_{x7}$ entering the dendrites and myr-tdTom-GFP(1-10) attached to the inner leaflet of dendritic membrane. Timestamp is relative to the first frame, with a 3-min interval between each frame.

Video 4. Cytoplasmic calcium dynamics in uninjured wildtype dendrites, related to Figure 7.

Time-lapse movie of an uninjured wildtype C4da neuron showing low baseline GCaMP6s signals and occasional local rises in dendrites. Timestamp is relative to the first frame, with a 3-min interval between each frame.

Video 5. Cytoplasmic calcium dynamics in dendrites of *Nmnat* KO neurons, related to Figure 7.

Time-lapse movie of a *Nmnat* KO C4da neuron showing calcium dynamics in uninjured dendrites. Timestamp is relative to the first frame, with a 3-min interval between each frame.

Video 6. Calcium dynamics in injured wildtype dendrites, related to Figure 7.

Time-lapse movie of laser-injured C4da dendrites from 1 to 11 hrs AI showing calcium dynamics in both severed dendrites and those attached to the soma. Timestamp is relative to the first frame, with a 3-min interval between each frame.

Video 7. AV-mCard labeling and calcium dynamics of injured dendrites, related to Figure 7.

719 Time-lapse movie of laser-injured C4da dendrites from 1 to 6 hrs AI showing labeling of injured
720 dendrites by the PS sensor AV-mCard and GCaMP6s signals. Timestamp is relative to the first frame,
721 with a 3-min interval between each frame.

722 **Video 8. Calcium dynamics in injured Wld^S OE dendrites, related to Figure 7.**

723 Time-lapse movie of laser-injured Wld^S OE C4da dendrites from 1 to 13 hours AI showing GCaMP6s
724 signals in severed dendrites. Timestamp is relative to the first frame, with a 3-min interval between each
725 frame.

726 **Video 9. Calcium dynamics in injured wildtype dendrites with a higher temporal resolution,**
727 **related to Figure 7.**

728 High temporal-resolution time-lapse movie of laser-injured wildtype C4da dendrites around 1 hr AI
729 showing calcium dynamics. Timestamp is relative to the first frame, with a 2-sec interval between each
730 frame.

731 **Video 10. Calcium dynamics in injured Wld^S OE dendrites at a higher temporal resolution,**
732 **related to Figure 7.**

733 High temporal-resolution time-lapse movie of laser-injured Wld^S OE C4da dendrites around 2 hrs AI
734 showing calcium dynamics. Timestamp is relative to the first frame, with a 2-sec interval between each
735 frame.

736 **Video 11. Irregular and infrequent cytoplasmic calcium flashes in injured Wld^S OE dendrites at a**
737 **higher temporal resolution, related to Figure 7.**

738 High temporal-resolution time-lapse movie of laser-injured Wld^S OE C4da dendrites around 2 hrs AI
739 showing irregular and infrequent GCaMP6s signals in severed dendrites. Timestamp is relative to the
740 first frame, with a 2-sec interval between each frame.
741

Key Resources Table

Designation	Source or reference	Identifiers	Additional information
Experimental Models: Organisms/Strains			
ppk-Gal4	Han et al., 2012		*ppk-Gal4* ^{VK00037}
UAS-CD4-tdTom	Han et al., 2011	RRID:BDSC_35841	*UAS-CD4-tdTom* ^{7M1}
ppk-CD4-tdTom	Han et al., 2011		*ppk-GFP(11)-CD4-tdTom* ^{2}
ppk-Cas9	Poe et al., 2019		*ppk-Cas9* ^{7D}
gRNA-Nmnat	this study		*gRNA-Nmnat* ^{VK00027}
ppk-LexA	Poe et al., 2017		*ppk-LexA.GAD* ^{3}
LexAop-Wld ^{S}	this study		*LexAop-WldS* ^{VK00027}
UAS-Wld $^{S\text{-}dead}$	Avery et al., 2009		
Sarm $^{-}$	Osterloh et al., 2012		*Sarm* ^{4705}
Sarm $^{-}$	Osterloh et al., 2012		*Sarm* ^{4621}
UAS-wnd	Bloomington Drosophila Stock Center	RRID:BDSC_51642	*UAS-wnd.C* ^{2}
UAS-Cas9	Bloomington Drosophila Stock Center	RRID:BDSC_58986	*UAS-Cas9.P2* ^{attP2}
drpr $^{-}$	Sapar et al., 2018		*drpr* ^{indel3}
UAS-JNK-RNAi	Bloomington Drosophila Stock Center	RRID:BDSC_57035	*TRiP.HMS04479* ^{attP40}
Dcg-Gal4	Sapar et al., 2018		
UAS-GFP-Lact	Sapar et al., 2018		*UAS-GFP-LactC1C2* ^{VK00018}
ppk-MApHS	Han et al., 2014		*ppk-MApHS* ^{1}
SOP-Cas9	Poe et al., 2019		*SOP-Cas9* ^{3A}
gRNA-Sarm	this study		*gRNA-Sarm* ^{VK00027}
R16A03-LexA	Sapar et al., 2018		*R16A03-LexAp65* ^{VK00027}
LexAop-GFP-LactC1C2	Sapar et al., 2018		*LexAop2-GFP-LactC1C2* ^{VK00033}
Or22a-Gal4	MacDonald et al., 2006		
UAS-mCD8-GFP	MacDonald et al., 2006		
ey-Cas9	this study		*ey-Cas9* ^{VK00005}
gRNA-axed	this study		*gRNA-axed* ^{VK00027}
gRNA-peb	this study		*gRNA-peb* ^{VK00027}
UAS-TMEM16F	Sapar et al., 2018		*UAS-TMEM16F(D430G)* ^{VK00016}
UAS-Wld ^{S}	MacDonald et al., 2006		
gRNA-CDC50	Sapar et al., 2018		*gRNA-CDC50* ^{attP2}
Df(drpr)	Bloomington Drosophila Stock Center	RRID:BDSC_9693	*Df(3L)BSC181*
UAS-SarmGOF	Neukomm et al., 2017		*UAS-Sarm* $^{\Delta Arm}$
UAS-JNK ^{DN}	Bloomington Drosophila Stock Center	RRID:BDSC_6409	*UAS-bsk.DN* ^{2}
LexAop-myr-tdTom-GFP(1-10)	this study		*LexAop2-myr-tdTom-GFP(1-10)* ^{VK00005}
UAS-sGFP(11)x7	this study		*UAS-sGFP(11)x7* ^{VK00027}
LexAop-myr-GCaMP6s	Akbergenova et al., 2018		*13xLexAop2-myr::GCaMP6s*
Gal4 $^{21\text{-}7}$	Song et al., 2007		
UAS-AnnexinV-mCard	Sapar et al., 2018		*UAS-AnnexinV-mCard* ^{VK00037}
Recombinant DNA			

Key Resources Table

pJFRC176-10XUAS-rox-dSTOP-rox-myr-GFP	Addgene	RRID:Addgene_32147	
pAC-U63-tgRNA-Rev	Poe et al., 2019	RRID:Addgene_112811	
pIHEU-sfGFP-LactC1C2	Sapar et al., 2018		
pAPLO-CD4-tdTom	Poe et al., 2017		
pDEST-APIC-Cas9	Poe et al., 2019	RRID:Addgene_121657	
pENTR11	Thermo Fisher Scientific,	#A10467	
Software and Algorithms			
Fiji	https://fiji.sc/	RRID: SCR_002285	
R	https://www.r-project.org/	RRID: SCR_001905	
Adobe Photoshop	Adobe	RRID:SCR_014199	
Adobe Illustrator	Adobe	RRID:SCR_010279	
Other			
Gateway™ LR Clonase™	Thermo Fisher Scientific,	#11791020	
NEBuilder® HiFi DNA Assembly Master Mix	New England Biolabs Inc.	#E2621	